

# 1 A 20-year (1998–2017) global sea surface dimethyl sulfide gridded 2 dataset with daily resolution

3 Shengqian Zhou<sup>1</sup>, Ying Chen<sup>1,2,3</sup>, Shan Huang<sup>4,5</sup>, Xianda Gong<sup>6,7</sup>, Guipeng Yang<sup>8,9,10</sup>, Honghai  
4 Zhang<sup>8,9,10</sup>, Hartmut Herrmann<sup>5</sup>, Alfred Wiedensohler<sup>5</sup>, Laurent Poulaïn<sup>5</sup>, Yan Zhang<sup>1,2</sup>, Fanghui Wang<sup>1</sup>,  
5 Zongjun Xu<sup>1</sup>, Ke Yan<sup>1</sup>

6 <sup>1</sup>Shanghai Key Laboratory of Atmospheric Particle Pollution Prevention, Department of Environmental Science &  
7 Engineering, Fudan University, Shanghai, 200438, China

8 <sup>2</sup>Institute of Eco-Chongming (IEC), National Observations and Research Station for Wetland Ecosystems of the Yangtze  
9 Estuary, Shanghai, 200062, China

10 <sup>3</sup>Institute of Atmospheric Sciences, Fudan University, Shanghai 200438, China

11 <sup>4</sup>Institute for Environmental and Climate Research, Jinan University, Guangzhou, 511443, China

12 <sup>5</sup>Leibniz Institute for Tropospheric Research, Leipzig, 04318, Germany

13 <sup>6</sup>Research Center for Industries of the Future, Westlake University, Hangzhou, 310030, China

14 <sup>7</sup>Key Laboratory of Coastal Environment and Resources of Zhejiang Province, School of Engineering, Westlake University,  
15 Hangzhou, 310030, China

16 <sup>8</sup>Frontiers Science Center for Deep Ocean Multispheres and Earth System, and Key Laboratory of Marine Chemistry Theory  
17 and Technology, Ministry of Education, Ocean University of China, Qingdao, 266100, China

18 <sup>9</sup>Laboratory for Marine Ecology and Environmental Science, Qingdao National Laboratory for Marine Science and  
19 Technology, Qingdao, 266071, China

20 <sup>10</sup>College of Chemistry and Chemical Engineering, Ocean University of China, Qingdao, 266100, China

21 *Correspondence to:* Ying Chen (yingchen@fudan.edu.cn)

22 **Abstract.** The oceanic emission of dimethyl sulfide (DMS) plays a vital role in the Earth's climate system and constitutes a  
23 substantial source of uncertainty in evaluating aerosol radiative forcing. Currently, the widely used monthly climatology of  
24 sea surface DMS concentration falls short of meeting the requirement for accurately simulating DMS-derived aerosols by  
25 chemical transport models. Hence, there is an urgent need for a high-resolution, multi-year global sea surface DMS dataset.  
26 Here we develop an artificial neural network ensemble model using 9 environmental factors as input features, which well  
27 captures the variabilities of DMS concentration across different oceanic regions. Subsequently, a global sea surface DMS  
28 concentration and flux dataset ( $1^\circ \times 1^\circ$ ) with daily resolution spanning from 1998 to 2017 is established. According to this  
29 dataset, the global annual average concentration was  $\sim 1.71$  nM, and the annual total emission was  $\sim 17.2$  TgS yr $^{-1}$ , with  $\sim 60\%$   
30 originating from the southern hemisphere. While overall seasonal variations are consistent with previous DMS climatologies,  
31 notable differences exist in regional-scale spatial distributions. The new dataset enables further investigations into daily and  
32 decadal variations. Throughout the period 1998–2017, the global annual average concentration exhibited a slight decrease,  
33 while total emissions showed no significant trend. The DMS flux from our dataset showed a stronger correlation with observed  
34 atmospheric methanesulfonic acid concentration compared to those from previous monthly climatologies. Therefore, it can  
35 serve as an improved emission inventory of oceanic DMS and has the potential to enhance the simulation of DMS-derived

36 aerosols and associated radiative effects. The new DMS gridded products are available at  
37 <https://doi.org/10.5281/zenodo.11879900> (Zhou et al., 2024).

## 38 1 Introduction

39 Dimethyl sulfide (DMS), primarily produced by ocean biota, accounts for more than half of natural sulfur emissions and  
40 significantly contributes to sulfur dioxide in the troposphere (Sheng et al., 2015; Andreae, 1990), which can be oxidized to  
41 sulfuric acid and form sulfate aerosols (Barnes et al., 2006; Hoffmann et al., 2016). Sulfate aerosols play an important role in  
42 climate systems by scattering solar radiation, changing cloud condensation nuclei (CCN) population, and altering cloud  
43 properties (Masson-Delmotte et al., 2021). Recent studies have proven that CCN over the remote ocean and polar regions are  
44 primarily composed of non-sea-salt sulfate ( $\text{nss-SO}_4^{2-}$ ) (Quinn et al., 2017; Park et al., 2021). Given the weak influence of  
45 anthropogenic  $\text{SO}_2$  over open oceans, marine biogenic DMS emerges as a crucial source of  $\text{nss-SO}_4^{2-}$ , regulating oceanic  
46 climate (McCoy et al., 2015). Accordingly, DMS has been suggested to be the key substance in the postulated feedback loop  
47 of marine phytoplankton to climate warming (the “CLAW” hypothesis) (Charlson et al., 1987), albeit facing several  
48 controversies (Quinn and Bates, 2011). To accurately simulate the climate effects of DMS-derived aerosols, high-fidelity and  
49 high-resolution data on sea surface DMS concentrations and emission fluxes are required, along with further exploration of  
50 complex atmospheric chemical and physical processes (Hoffmann et al., 2016; Novak et al., 2021). It has been indicated that  
51 the uncertainty in DMS emission flux is the second largest contributor to the overall uncertainty associated with natural  
52 aerosols in evaluating the aerosol indirect radiative forcing (Carslaw et al., 2013). Therefore, understanding the spatiotemporal  
53 variations of DMS in global oceans is currently an important task.

54 There are complex production and consumption mechanisms of DMS in the upper ocean, which makes it difficult to well  
55 capture the dynamics and distributions of sea surface DMS across different regions. Dimethylsulfoniopropionate (DMSP), the  
56 major precursor of DMS, is synthesized mainly by phytoplankton in the photic zone and plays a variety of physiological  
57 functions in algal cells (Stefels, 2000; Sunda et al., 2002; McParland and Levine, 2018). The DMSP yield varies significantly  
58 among algal species (Stefels et al., 2007; Keller et al., 1989), and DMS can be produced through DMSP intracellular and  
59 extracellular cleavage by both algae and bacteria (Alcolombri et al., 2015; Zhang et al., 2019). Therefore, the oceanic DMS  
60 produced via multiple pathways can be affected by many biotic and abiotic factors, including temperature, salinity, solar  
61 radiation, mixed layer depth, nutrients, oxygen, acidity, etc. (Simó and Pedrós-Alió, 1999a; Vallina and Simó, 2007; Stefels,  
62 2000; Zindler et al., 2014; Six et al., 2013; Omori et al., 2015; Stefels et al., 2007). In addition, seawater DMS undergoes  
63 various removal pathways (bacterial consumption, photodegradation, sea-to-air ventilation, etc.), further complicating its  
64 cycling (Stefels et al., 2007; Galí and Simó, 2015; Hopkins et al., 2023). Therefore, although previous studies have developed  
65 several empirical algorithms (Simó and Dachs, 2002; Belviso et al., 2004b; Vallina and Simó, 2007) and process-embedded  
66 prognostic models (Kloster et al., 2006; Vogt et al., 2010; Belviso et al., 2011; Wang et al., 2015) based on relevant variables

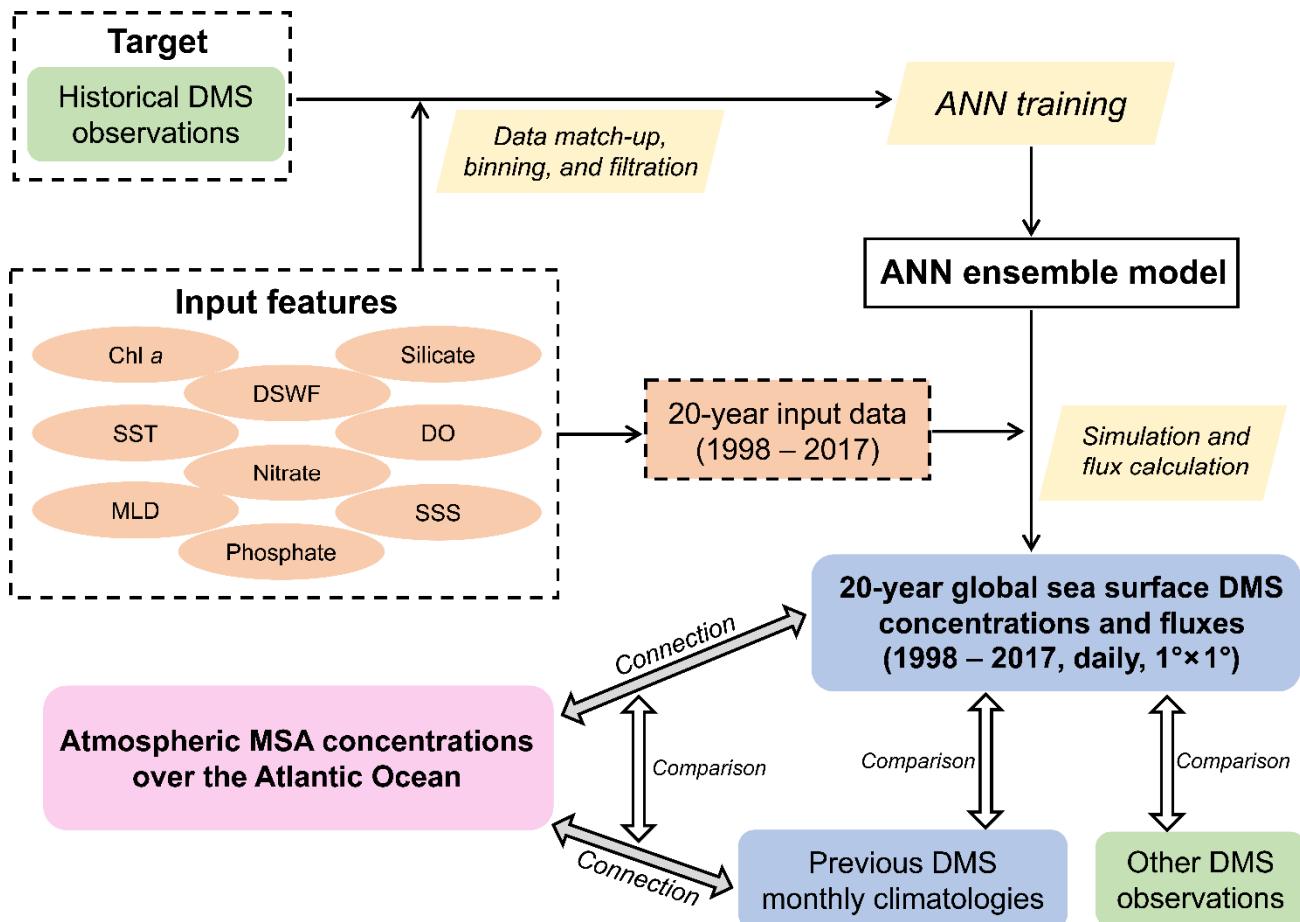
67 (mixed layer depth, chlorophyll *a*, nutrients, radiation, phytoplankton group, etc.) to estimate the distribution of DMS, their  
68 results showed significantly different patterns and inconsistency with observations in many regions (Tesdal et al., 2016;  
69 Belviso et al., 2004a). Recently, Galí et al. (2018) developed a new empirical algorithm following a parameterization of DMSP  
70 (Galí et al., 2015). The estimated DMS field exhibited a generally higher consistency with observations than those derived  
71 from previous algorithms SD02 (Simó and Dachs, 2002) and VS07 (Vallina and Simó, 2007), but this method did not consider  
72 the influences of nutrients and still exhibited substantial biases in certain regions (e.g., near the Antarctic).

73 Since Lovelock et al. (1972) first discovered the ubiquitous presence of DMS in seawater, numerous observations of sea  
74 surface DMS have been conducted worldwide, yielding a substantial volume of observational data to date. Based on these  
75 worldwide measurements, monthly climatology of global DMS can be generated through interpolation and extrapolation  
76 (Hulswar et al., 2022; Kettle et al., 1999; Lana et al., 2011). The latest version incorporated 873,539 raw observations (48,898  
77 after data filtration and unification for climatology development), and the estimated global annual mean concentration and  
78 total flux are 2.26 nM and 27.1 TgS yr<sup>-1</sup>, respectively (Hulswar et al., 2022). However, despite the abundance of data,  
79 significant spatial and temporal disparities persist, potentially introducing large uncertainties in regions or periods with sparse  
80 observations. Furthermore, the observational data from different years within a particular month were combined together for  
81 interpolation and extrapolation, and the interannual variations cannot be investigated by this approach.

82 In recent years, the application of data-driven approaches like machine learning to Earth system science has drawn more and  
83 more attention. Compared with traditional approaches, machine learning explores larger function space and captures more  
84 hidden information from the big data, hence it often provides a better prediction performance (Reichstein et al., 2019; Zheng  
85 et al., 2020; Bergen et al., 2019). For instance, a recent study demonstrated that artificial neural network (ANN) can capture  
86 much more (~66%) of the raw data variance than multilinear regression (~39%), and a global monthly climatology of sea  
87 surface DMS concentration has been developed based on ANN model (Wang et al., 2020). The machine learning techniques  
88 have also been used to simulate the distribution of DMS in the Arctic (Humphries et al., 2012; Qu et al., 2016), North Atlantic  
89 Ocean (Bell et al., 2021; Mansour et al., 2023), Northeast Pacific Ocean (McNabb and Tortell, 2022), Southern Ocean  
90 (McNabb and Tortell, 2023), and East Asia (Zhao et al., 2022).

91 However, to our best knowledge, there is currently no global-scale sea surface gridded DMS dataset with both high time  
92 resolution (daily) and long-term coverage (> 10 years). Such a dataset is urgently needed for modeling the atmospheric  
93 processes and climatic implications of oceanic DMS. The sea surface concentration and sea-to-air emission flux of DMS can  
94 vary greatly from day to day (Simó and Pedrós-Alió, 1999b), and the emitted DMS exerts effects on the atmosphere over time  
95 scales of several hours to days. Relying solely on monthly climatology of DMS as the emission inventory may fail to capture  
96 important details and could lead to large modeling biases compared to observed concentrations of atmospheric DMS or its  
97 oxidation products (Chen et al., 2018; Fung et al., 2022).

98 Here, we build a 20-year (1998 – 2017) global sea surface DMS gridded dataset ( $1^\circ \times 1^\circ$ ) with a daily resolution based on a  
 99 data-driven machine learning approach (ANN ensemble). This product can improve our understanding of the spatiotemporal  
 100 variations of oceanic DMS. More importantly, it can serve as an updated emission inventory of marine biogenic DMS for  
 101 chemical transport models, which is beneficial for enhancing the simulation of atmospheric processes of DMS and reducing  
 102 the uncertainties in marine aerosol's climate effects. The paper consists of four main parts as depicted in Fig. 1: (1) the  
 103 development of machine learning model based on global DMS measurements and 9 ancillary environmental variables; (2) the  
 104 derived spatial and temporal distributions of DMS and comparisons with previous estimates; (3) an example showing the  
 105 superiority of our newly developed DMS field through its correlation with atmospheric biogenic sulfur; and (4) the  
 106 uncertainties and limitations inherent in our approach and the resulting data product.



107  
 108 **Figure 1.** Flowchart of this study, including the development of ANN ensemble model, construction of new DMS gridded  
 109 dataset, and subsequent evaluations of this product.

110 **2 Methodology**

111 **2.1 Input datasets**

112 The in-situ DMS measurement data used for training the machine learning model primarily sourced from the Global Surface  
113 Seawater DMS (GSSD) database (Kettle et al., 1999). The GSSD database contains a total of 87,801 DMS measurements  
114 collected across 266 cruise and fixed-site observation campaigns from 11 March 1972 to 27 August 2017  
115 (<https://saga.pmel.noaa.gov/dms/>, last access: 1 April 2020). Hulswar et al. (2022) consolidated other DMS measurements not  
116 included in the GSSD database to establish an updated DMS climatology. Here we incorporated these additional data predating  
117 2017, originating from 8 campaigns (number of samples = 6,711). The spatial distribution of these combined 94,512 in-situ  
118 observational data is shown in Fig. S1, which covers all major regions of the global ocean.

119 We selected 9 environmental variables relevant to DMS biogeochemical processes as input features, including chlorophyll *a*  
120 (Chl *a*), sea surface temperature (SST), mixed layer depth (MLD), nitrate, phosphate, silicate, dissolved oxygen (DO),  
121 downward short-wave radiation flux (DSWF), and sea surface salinity (SSS). The data sources and relevant information of  
122 these 9 input variables and DMS are listed in Table 1. Chl *a* data were obtained from both in-situ observations, co-located with  
123 DMS data, and satellite remote sensing products (Copernicus-GlobColour, Level-4, daily,  $0.042^\circ \times 0.042^\circ$ ). The Copernicus-  
124 GlobColour Level-4 dataset integrates multiple upstream sensors including SeaWiFS, MODIS-Aqua & Terra, MERIS, VIIRS-  
125 SNPP & JPSS1, and OLCI-S3A & S3B, with an interpolation procedure applied to fill missing data (Garnesson et al., 2019).  
126 Daily SST data ( $0.25^\circ \times 0.25^\circ$ ) were from the NOAA OI SST V2 high-resolution blended reanalysis dataset (Huang et al.,  
127 2021). Daily MLD, DSWF, and SSS were from the modeling outputs of NASA's "Estimating the Circulation and Climate of  
128 the Ocean" (ECCO) consortium, Version 4 Release 4 (V4r4) (Forget et al., 2015). The sea surface concentrations of nitrate,  
129 phosphate, silicate, and DO were from the CMEMS global biogeochemical multi-year hindcast dataset (daily,  $0.25^\circ \times 0.25^\circ$ ).  
130 The surface wind speed (WS) and sea ice fraction (SI) data are needed in the calculation of sea-to-air flux (details are provided  
131 in Section 2.4.2). Here we utilized the daily 10-meter WS data from ECCO V4r4 and the daily SI data from NOAA OI SST  
132 V2. Since there are multiple different spatial grids among all datasets, the data match-up has been conducted as described in  
133 the next section.

134

135 **Table 1.** The data sources and relevant information of variables used for model development, DMS simulation, and flux  
 136 calculation

Variable	Data source	URL	Temporal resolution	Temporal coverage	Spatial grid
DMS	GSSD database	<a href="https://saga.pmel.noaa.gov/dms/">https://saga.pmel.noaa.gov/dms/</a>	In-situ	Mar. 1972 – Aug. 2017	-
	Other campaigns integrated in Hulswart et al. (2022)	<a href="https://data.mendeley.com/datasets/hyn62spny2/1">https://data.mendeley.com/datasets/hyn62spny2/1</a>	In-situ	Feb. 2000 – Jun. 2016	-
Chl <i>a</i>	GSSD database	<a href="https://saga.pmel.noaa.gov/dms/">https://saga.pmel.noaa.gov/dms/</a>	In-situ	Oct. 1980 – Aug. 2017	-
	Copernicus-GlobColour Level-4	<a href="https://data.marine.copernicus.eu/product/OCEANCOLOR_GLO_BGC_L4_MY_009_104/description">https://data.marine.copernicus.eu/product/OCEANCOLOR_GLO_BGC_L4_MY_009_104/description</a>	Daily	Sep. 1997 – present	0.042°×0.042°
CMEMS	CMEMS global biogeochemical multi-year hindcast (only used for the simulation of DMS concentration in polar regions when satellite Chl <i>a</i> is unavailable)	<a href="https://data.marine.copernicus.eu/product/GLOBAL_MULTIYEAR_BGC_001_029/description">https://data.marine.copernicus.eu/product/GLOBAL_MULTIYEAR_BGC_001_029/description</a>	Daily	Jan. 1993 – present	0.25°×0.25°
	SST	<a href="https://psl.noaa.gov/data/gridded/data.noaa.oisst.v2.hi.ghres.html">https://psl.noaa.gov/data/gridded/data.noaa.oisst.v2.hi.ghres.html</a>	Daily	Sep. 1981 – present	0.25°×0.25°
MLD					
DSWF	NASA ECCO V4r4	<a href="https://data.nas.nasa.gov/ecco/data.php?dir=/eccodata/lle_90/ECCOv4/Release4">https://data.nas.nasa.gov/ecco/data.php?dir=/eccodata/lle_90/ECCOv4/Release4</a>	Daily	Jan. 1992 – Dec. 2017	LLC90 (22 – 110 km)
SSS					
Nitrate					
Phosphate	CMEMS global biogeochemical multi-year hindcast	<a href="https://data.marine.copernicus.eu/product/GLOBAL_MULTIYEAR_BGC_001_029/description">https://data.marine.copernicus.eu/product/GLOBAL_MULTIYEAR_BGC_001_029/description</a>	Daily	Jan. 1993 – present	0.25°×0.25°
Silicate					
DO					
WS	NASA ECCO V4r4	<a href="https://data.nas.nasa.gov/ecco/data.php?dir=/eccodata/lle_90/ECCOv4/Release4">https://data.nas.nasa.gov/ecco/data.php?dir=/eccodata/lle_90/ECCOv4/Release4</a>	Daily	Jan. 1992 – Dec. 2017	LLC90 (22 – 110 km)
SI	NOAA OI SST V2	<a href="https://psl.noaa.gov/data/gridded/data.noaa.oisst.v2.hi.ghres.html">https://psl.noaa.gov/data/gridded/data.noaa.oisst.v2.hi.ghres.html</a>	Daily	Sep. 1981 – present	0.25°×0.25°

137

## 138 **2.2 Data preprocessing for model development**

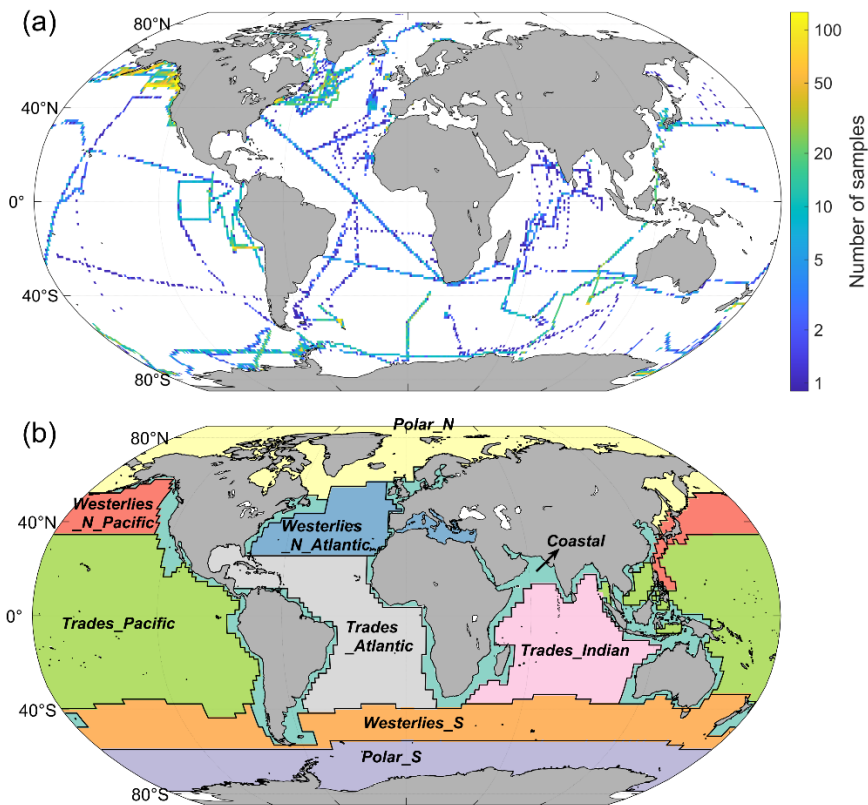
139 The data extraction and match-up were performed based on the sampling location and time associated with each DMS  
 140 measurement record, as well as the temporal range and grid distribution of each variable. For satellite-retrieved Chl *a*, the data  
 141 of the grids covering DMS sampling locations were extracted. If the data of the corresponding grid is missing, the average

142 value of the  $5 \times 5$  grids nearby was calculated and used. For other variables, only values in the grids matching the DMS sampling  
143 locations were extracted.

144 There are in-situ Chl  $a$  measurements co-located with certain GSSD data. They were also used along with satellite-retrieved  
145 Chl  $a$ . In-situ Chl  $a$  measurements with low precision (defined as  $< 0.1 \text{ mg m}^{-3}$ , and the number of significant digits is 1) were  
146 removed. For a specific in-situ observation campaign, if the number of low-precision values is larger than 10 and accounts for  
147 more than half, all in-situ Chl  $a$  data from this campaign were excluded. In addition, the in-situ Chl  $a$  data in the GSSD database  
148 were measured by two different methods: Turner fluorometry and high-performance liquid chromatography (HPLC). In order  
149 to improve mutual consistency, a conversion between the data from these two methods was applied and then the in-situ Chl  $a$   
150 concentrations were adjusted to match up with satellite Chl  $a$  following the functions described in Galí et al. (2015). After that,  
151 the statistical outliers for all  $\log_{10}(\text{Chl } a)$  (outside the range of average  $\pm 3$  standard deviations) were eliminated. The  
152 comparison between in-situ and satellite-retrieved Chl  $a$  data is shown in Fig. S2. A strong consistency between in-situ and  
153 daily satellite Chl  $a$  data ( $R^2 > 0.5$ , RMSE  $< 0.4$ ) suggests the rationale for integrating these datasets. The  $\log_{10}$  transformation  
154 was applied to make the data distribution close to normal distribution. When finally selecting the  $\log_{10}(\text{Chl } a)$  corresponding  
155 to each DMS data, in-situ data were prioritized where available; otherwise, the satellite-retrieved data were used.

156 DMS and extracted MLD and three nutrients (nitrate, phosphate, silicate) were also performed  $\log_{10}$  transformation. The  
157 statistical outliers of each variable were excluded as mentioned above. After data filtration, a total of 633,361 samples with  
158 valid data for all variables were obtained. To avoid data aggregation bias stemming from multiple data points gathered within  
159 a narrow temporal and spatial range (i.e., the same day and within a region smaller than  $0.05^\circ \times 0.05^\circ$ ), these data points were  
160 averaged. Consequently, 41,157 binned samples were utilized for subsequent model development, with their spatial  
161 distribution depicted in Fig. 2a.

162 We divided the global ocean into 9 regions based on Longhurst's biomes (Longhurst, 1998). There are 6 biomes in  
163 Longhurst's definition, including Coastal, Polar\_N, Polar\_S, Westerlies\_N, Westerlies\_S, and Trades (the .shp file of  
164 Longhurst's biomes and provinces was downloaded from <https://www.marineregions.org/downloads.php#longhurst>). We  
165 further divided Westerlies\_N into Westerlies\_N\_Pacific and Westerlies\_N\_Atlantic, and divided Trades into Trades\_Pacific,  
166 Trades\_Indian, and Trades\_Atlantic by different oceanic basins, as shown in Fig. 2b. It is noteworthy that there are 11,237  
167 samples in the Coastal region, constituting 27.3% of the entire sample set, despite the Coastal biome accounting for only  
168 9.7% of the global ocean area. Given the distinct seawater physiochemical and biological conditions in coastal seas  
169 compared to other regions, the disproportionately higher density of samples within the Coastal biome might cause the model  
170 to overly prioritize this region. To mitigate this data imbalance and ensure the model captures broader patterns in open  
171 oceans, we adjusted the data distribution during model training and validation processes. Specifically, for each training  
172 session, a portion of coastal samples is randomly removed, ensuring the proportion of coastal samples in the total sample set  
173 (denoted as  $F_{\text{coastal}}$ ) matches its area proportion.



174  
175  
176  
177

**Figure 2.** (a) The distribution of 41,157 DMS observational data after matchup, filtration, and binning for constructing the ANN model. The grid size is  $1^\circ \times 1^\circ$ . (b) Nine oceanic regions separated based on Longhurst's biomes (Longhurst, 1998).

### 178 2.3 Artificial neural network training and validation

179 The 41,157 binned samples after the previously mentioned data preprocessing were used to develop the artificial neural  
180 network (ANN) model. The target feature is  $\log_{10}(\text{DMS})$ , and the input features are  $\log_{10}(\text{Chl } a)$ , SST,  $\log_{10}(\text{MLD})$ ,  
181  $\log_{10}(\text{nitrate})$ ,  $\log_{10}(\text{phosphate})$ ,  $\log_{10}(\text{silicate})$ , DO, DSWF, and SSS. The data of all variables were standardized before  
182 training.

183 We randomly selected 10% of the samples ( $n = 4,116$ ) to be entirely excluded from training, as a testing subset for global  
184 validation and overfitting test. Specifically, 401 samples were randomly selected from Coastal biome, and 3,715 samples were  
185 selected from other biomes to compose the testing subset, matching the proportion of coastal area in global oceans (9.7%).  
186 Then, the remaining samples ( $n = 37,041$ ) were utilized for training and cross validation, with a constraint of  $F_{\text{coastal}}$  equal to  
187 9.7% in each training session as mentioned above.

188 Our feedforward fully connected neural network comprises two hidden layers, with 15 nodes in each layer. The activation  
189 functions for the first and second layers are ReLU and tanh, respectively. We applied L2 regularization (lambda = 1E-4) to  
190 counteract overfitting. The loss function is mean square error (MSE). Training stops if the validation loss is greater than or  
191 equal to the minimum validation loss computed so far 20 times in a row. The training processes were carried out with Statistics  
192 and Machine Learning Toolbox on Matlab 2022b. We repeated the data split (for training and validation sets) and training  
193 processes for 100 times and obtained 100 neural networks. The average prediction results of multiple ANNs shows a much  
194 higher consistency with the observations than a single ANN (Fig. S3). As the number of ANNs ( $N_{\text{training}}$ ) increases, the accuracy  
195 of model predictions initially improves and then stabilizes. We adopted the average output of 20 ANNs as the final output,  
196 balancing performance and computational costs effectively. This kind of multiple-training approach, often termed “ANN  
197 ensemble” or “Monte Carlo cross-validation”, has been widely used to improve the model generalization and performance  
198 (Sigmund et al., 2020; Holder et al., 2022) as well as get a better model evaluation (Dubitzky et al., 2007).

199

## 200 **2.4 Deriving the 20-year global DMS distributions**

### 201 **2.4.1 Simulation of sea surface DMS concentrations**

202 First, we constructed the daily gridded dataset of input variables with a spatial resolution of  $1^\circ \times 1^\circ$  from 1998 to 2017 based  
203 on the data sources listed in Table 1 (except in-situ Chl  $a$  data). Datasets with a higher spatial resolution than  $1^\circ \times 1^\circ$  were  
204 binned into  $1^\circ \times 1^\circ$ . In polar regions, the satellite Chl  $a$  data are missing during winter, and the Chl  $a$  data from CMEMS global  
205 biogeochemical multi-year hindcast were used to fill the missing values. Then, the obtained gridded dataset was fed into the  
206 ANN ensemble model, and the 20-year global distribution of sea surface DMS concentration with daily resolution was  
207 simulated.

### 208 **2.4.2 Calculation of sea-to-air fluxes**

209 The sea-to-air fluxes of DMS were calculated on the basis of simulated surface DMS concentrations following equation (1):

$$210 \quad DMS \text{ flux} = Kt \times (DMS_w - \frac{DMS_a}{H}) \quad (1)$$

211 Here  $DMS_w$  and  $DMS_a$  are DMS concentrations in surface seawater and air, respectively.  $H$  is Henry’s law constant of DMS.  
212 Since  $\frac{DMS_a}{H}$  is usually  $\ll DMS_w$ , this term was omitted in the calculation.  $Kt$  is the total transfer velocity considering the sea  
213 ice coverage fraction ( $SI$ ):

$$214 \quad Kt = k_t \times (1 - SI) \quad (2)$$

215  $k_t$  is the total transfer velocity without considering sea ice which is calculated by equation (3):

$$216 \quad \frac{1}{k_t} = \frac{1}{k_w} + \frac{1}{k_a \times H} \quad (3)$$

217 Here  $k_w$  and  $k_a$  are the water-side transfer velocity and air-side transfer velocity, respectively. We used the same approach as  
218 Galí et al. (2019) to obtain  $k_w$ ,  $k_a$ , and  $H$  for DMS, where the effect of wind speed was considered for  $k_a$ , and the influences of  
219 SST and SSS were considered for  $H$ . The calculations of  $k_a$  and  $H$  followed the parameterizations of Johnson (2010). As for  
220  $k_w$  calculation, we adopted the bubble scheme (Woolf, 1997), which divided the sea-to-air mass transfer process into  
221 turbulence- and bubble-mediated gas exchange. The calculated  $k_w$  based on the bubble scheme is lower than that of  
222 Nightingale's scheme (Nightingale et al., 2000) under conditions of high wind speed, exhibiting a smaller deviation from the  
223 measurements (Beale et al., 2014; Galí et al., 2019). Before calculation, WS and SI data were also binned by  $1^\circ \times 1^\circ$  grid. By  
224 using WS and SI together with SST and SSS datasets, we obtained the daily gridded  $Kt$  and then calculated the sea-to-air DMS  
225 fluxes (daily, 1998–2017) by multiplying simulated DMS concentrations by  $Kt$  values.

## 226 3 Results

### 227 3.1 Model performance

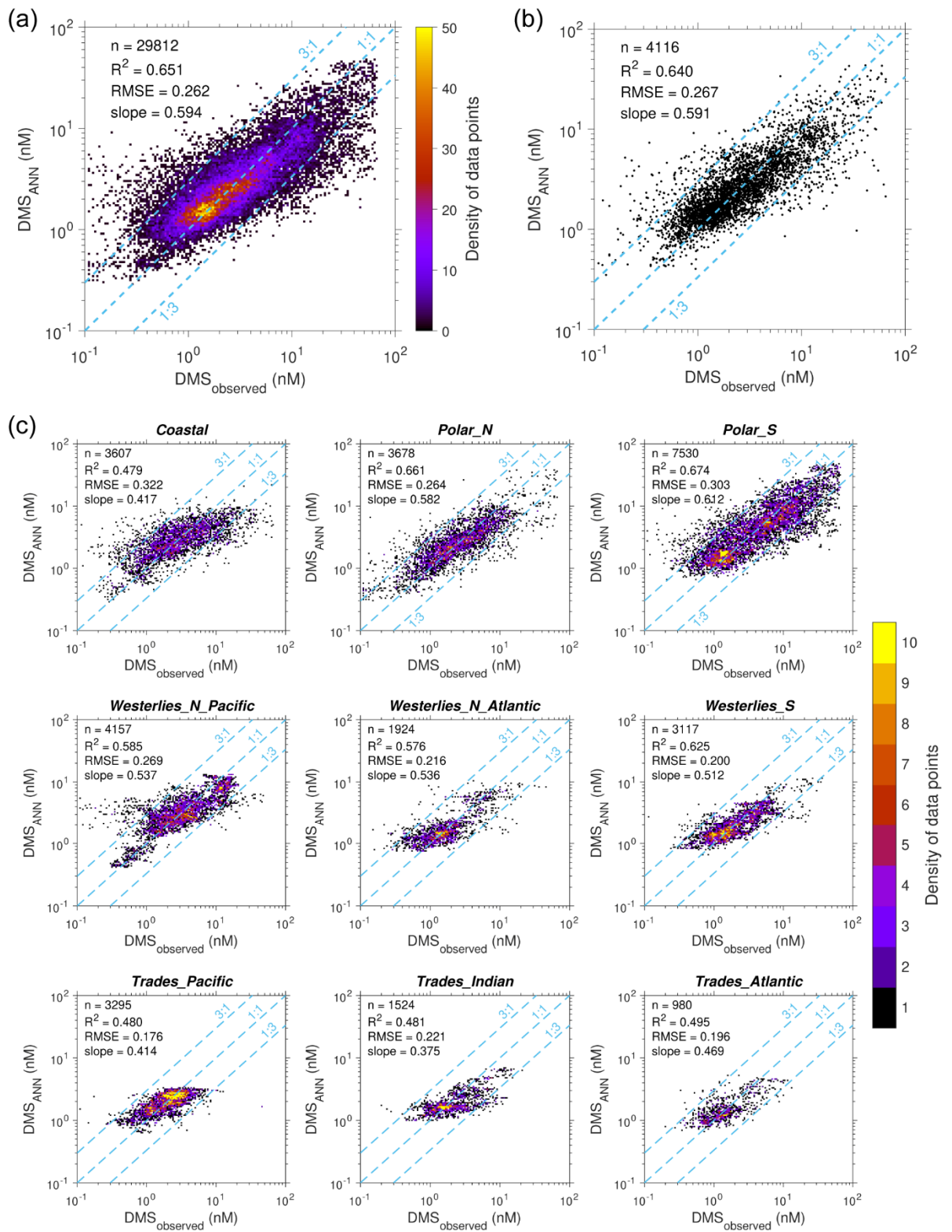
228 As shown in Fig. 3a, the newly developed ANN ensemble model captures a substantial part of data variance globally ( $\log_{10}$   
229 space  $R^2 = 0.651$  and  $\text{RMSE} = 0.262$ ). 92.8% of ANN simulated concentration values fall within 1/3 to 3 times of corresponding  
230 true values. The performance for testing set ( $R^2 = 0.640$ ,  $\text{RMSE} = 0.267$ , and 92.7% of data within the range of 1/3 to 3 times  
231 of observations) is very close to that for the training set (Fig. 3b), suggesting no obvious overfitting. The ANN model exhibits  
232 better performance compared to previous empirical and process-based models ( $R^2 = 0.01\text{--}0.14$ ) (Tesdal et al., 2016) as well  
233 as the satellite-based algorithm ( $R^2 = 0.50$ ) (Galí et al., 2018). The ANN model developed by Wang et al. (2020) showed a  
234 similar performance ( $R^2 = 0.66$ ,  $\text{RMSE} = 0.264$  for training set) to our model, despite their more complex ANN configuration  
235 (two hidden layers with 128 nodes each) and the inclusion of sample location and time into input features. However, the more  
236 complex model will significantly increase the computational cost, and the incorporation of location and time information may  
237 weaken the physical interpretability.

238 The performance of the model was evaluated across each of the nine oceanic regions. As illustrated in Fig. 3c and 4, the  $\log_{10}$   
239 space RMSEs are all below 0.32 (equivalent to a concentration ratio of 2.09 in linear space), except for the Coastal region  
240 (training:  $\text{RMSE} = 0.322$ ,  $R^2 = 0.479$ ; testing:  $\text{RMSE} = 0.332$ ,  $R^2 = 0.480$ ). Since the Coastal region comprises only 9.7% of  
241 the global oceanic area, the comparatively lower performance in this area has minimal impact on the overall ability to predict  
242 the spatiotemporal distributions of DMS on a global scale. Despite the  $R^2$  values in Trades\_Pacific and Trades\_Atlantic being  
243 lower than 0.5, which is related to the relatively narrow variation range of DMS concentration, the RMSEs in these regions  
244 remain quite low and comparable to those of other regions. In general, our ANN ensemble model demonstrates a satisfactory  
245 capacity to reproduce variations in DMS concentrations across diverse oceanic regions.

246 However, it is noteworthy that our model tends to underestimate extremely high DMS concentrations and overestimate  
247 extremely low concentrations. Overall, the linear regressions between ANN-predicted and observed DMS concentrations yield  
248 slopes significantly lower than unity across all regions (Fig. 3c and 4), and there are significantly positive correlations between  
249 prediction residuals (observation – prediction) and observed  $\log_{10}(\text{DMS})$  (Fig. S5 and S6). From a data perspective, this may  
250 be partly due to the insufficient number of samples with extreme DMS concentrations (known as underrepresentation), making  
251 it difficult to adequately capture the relevant information during training process. To test this point, we adopted a weighted  
252 resampling strategy to bolster the number of samples in the minority class before training, which has been widely used in  
253 machine learning to deal with the data imbalance issue (Haibo et al., 2008; Yu and Zhou, 2021; Chawla et al., 2002). The basic  
254 idea is to set a higher probability of being sampled for the minority class with extreme DMS concentrations, and the details  
255 are illustrated in Fig. S7 and explained in Appendix B. The results indicate that the weighted resampling scheme cannot fully  
256 alleviate the model bias. Although it does elevate the overall prediction-versus-observation slopes from  $\sim 0.59$  to  $\sim 0.63$ , this  
257 improvement is marginal (Fig. S8 and S9). In several regions like Westerlies\_S and Trades biomes, the slopes are even lower  
258 than original values. Furthermore, the data become more scattered after implementing the weighted resampling, resulting in  
259 increased RMSE and decreased  $R^2$ . Therefore, there are other potential issues causing the model bias, which are discussed in  
260 Section 4. The original model, trained without weighted resampling, was adopted for subsequent analysis and the construction  
261 of the gridded DMS dataset.

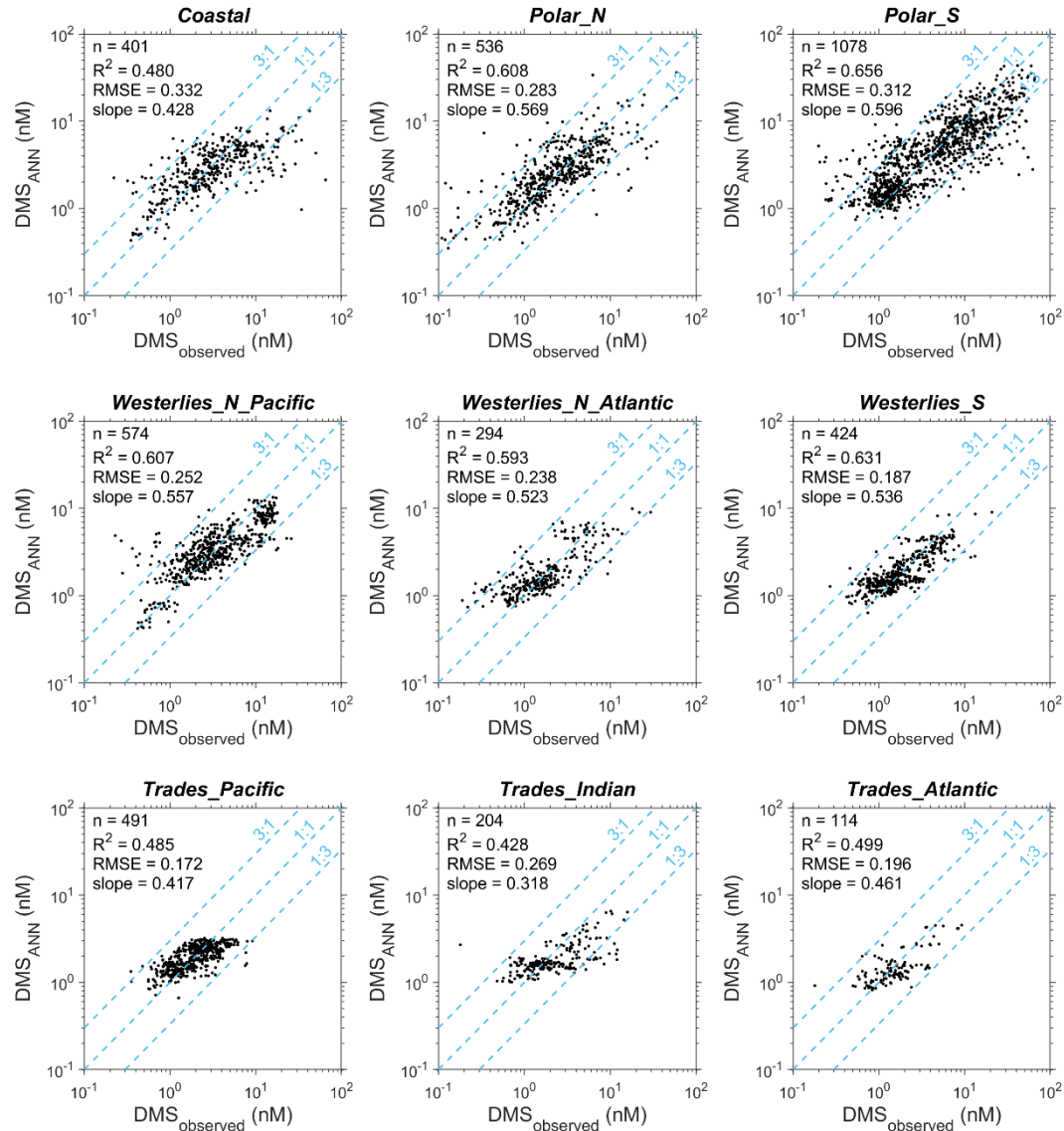
262 Primarily owing to the underestimation of high DMS concentrations, a negative mean bias (MB) in DMS concentration is  
263 evident across all regions, ranging from  $-0.18$  to  $-2.02$  nM (Table 2). The normalized mean bias (NMB, the ratio between mean  
264 bias and mean observed concentration) ranges from  $-8.7\%$  to  $-32.2\%$ . The most significant NMB emerges in Coastal and  
265 Trades\_India regions, while NMB remains within  $-25\%$  for other regions. The global MB and NMB are  $-1.05$  nM and  $-22.1\%$ ,  
266 respectively. It is worth noting that these biases are compared against historical DMS observations, which were conducted  
267 within a very limited geographical area and time periods. Thus, they cannot be interpreted as the actual mean modelling bias  
268 for the entire region. On the other hand, the negative biases at high end of the concentrations are partially cancelled out by the  
269 positive biases at low end during the averaging over the entire region. The bias at a specific grid could be much larger.  
270 Nevertheless, those extreme DMS concentrations ( $> 15$  nM or  $< 0.3$  nM), exhibiting the most significant modeling bias,  
271 represent only a minority of the entire sample set (6.9%). Our model adeptly reproduces the majority of observations with  
272 moderate DMS concentrations across all regions, with the percentage of predicted values falling within 1/3 to 3 times of  
273 observations ranging from 87.0% to 98.8%.

274



276 **Figure 3.** Comparisons between ANN-simulated and observed DMS concentrations. (a) Scatter density for simulated versus  
 277 observed DMS concentrations of the samples used in ANN training. (b) Comparison between the simulated versus observed  
 278 DMS concentrations of testing set. (c) Comparison between the simulated versus observed DMS concentrations of the samples  
 279 used in ANN training across 9 regions. The number of data points (n),  $\log_{10}$  space  $R^2$ , root mean square error (RMSE), and  
 280 linear regression slope are also displayed.

281



282

283 **Figure 4.** Comparisons between the simulated versus observed DMS concentrations of the testing set across 9 regions.

284

285

286 **Table 2.** The mean bias and normalized mean bias of the ANN-predicted DMS concentrations against observations across  
 287 different regions.

Region	Mean bias (nM)	Normalized mean bias
Coastal	-1.55	-32.2%
Polar_N	-0.90	-21.4%
Polar_S	-2.02	-24.1%
Westerlies_N_Pacific	-0.91	-18.8%
Westerlies_N_Atlantic	-0.24	-10.4%
Westerlies_S	-0.36	-14.1%
Trades_Pacific	-0.19	-8.7%
Trades_Indian	-0.73	-26.7%
Trades_Atlantic	-0.18	-10.1%
Global	-1.05	-22.1%

288

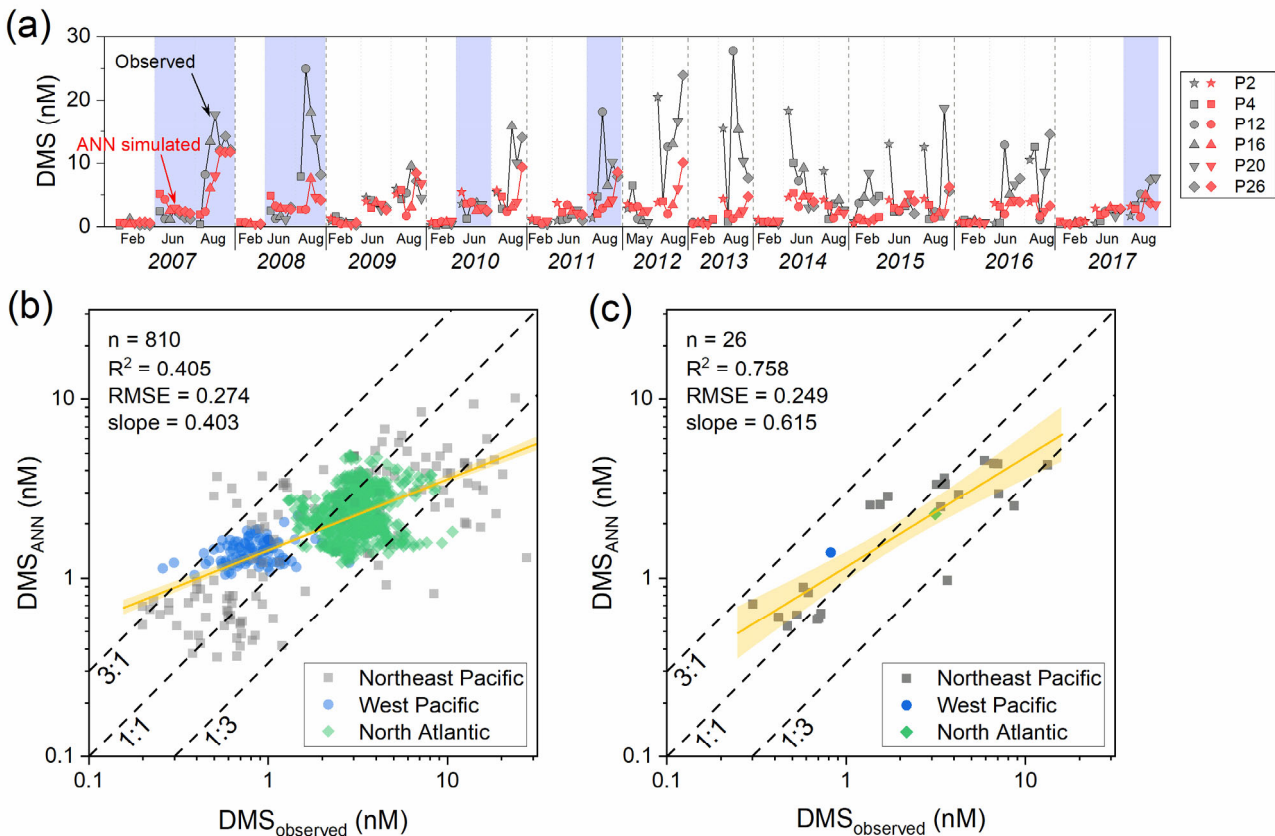
289

290 It is worth noting that there may be intrinsic connections between the 10% excluded testing subset and the training set, because  
 291 the data from the same cruise or fixed-site campaign have certain continuity. To further evaluate the reliability of the ANN  
 292 model, we compared the simulated DMS concentrations with the observational data from fully independent campaigns, which  
 293 are obtained from 33 cruises in Northeast Pacific, West Pacific, and North Atlantic (number of data = 6,478). These data  
 294 include (1) discrete sampling and measurement during 31 cruises of *Line P Program* in Northeast Pacific (Steiner et al., 2011)  
 295 (9 February 2007 – 26 August 2017, number of data = 177, <https://www.waterproperties.ca/linep/index.php>, last access: 23  
 296 November 2020), (2) underway measurements during *SONNE cruise 202/2 (TRANSBROM)* in West Pacific (Zindler et al.,  
 297 2013) (9 – 23 October 2009, number of data = 115, <https://doi.org/10.1594/PANGAEA.805613>, last access: 23 November  
 298 2020), (3) underway measurements during the third *North Atlantic Aerosols and Marine Ecosystems Study (NAAMES)*  
 299 campaign (Behrenfeld et al., 2019; Bell et al., 2021) (6 – 24 September 2017, number of data = 1,025,  
 300 <https://seabass.gsfc.nasa.gov/naames>, last access: 27 November, 2020). Before the comparison, the data measured within a  
 301 0.05°×0.05° grid and at the same day were binned by arithmetic average.

302 The comparisons between these observed DMS concentrations and ANN simulation are shown in Fig. 5. Regarding the *Line*  
 303 *P Program*, it should be noted that there are 7 cruises included in the GSSD database, but those data were obtained by underway  
 304 measurements, different from the discrete sampling (Niskin bottle) data used here. Hence, these cruises were retained and  
 305 marked in Fig. 5a but excluded in subsequent statistical analysis (Fig. 5b-c). It can be seen that the model effectively captures  
 306 the seasonal variation in Northeast Pacific, which is generally August > June > February (Fig. 5a). However, the small-scale  
 307 spatial variations can only be partially reproduced by the model in certain campaigns, such as those in June and August of  
 308 2007, June of 2009, August of 2012, and August of 2016. Notably, the model generally underestimates high DMS

309 concentrations during summer, particularly those exceeding 10 nM, consistent with earlier discussions. Aggregating data from  
 310 all campaigns across three regions, the  $\log_{10}$  space RMSE of simulated DMS concentrations against observations is 0.274,  
 311 marginally higher than the training set. Most simulated values (93.0%) are within the range of 1/3 to 3 times of observations.  
 312 The results further evidence that there is no significant overfitting in our model. When data from each campaign are binned,  
 313 simulations demonstrate high consistency with observations, as depicted in Fig. 5c (RMSE = 0.249,  $R^2 = 0.758$ ). In summary,  
 314 although our ANN ensemble model may not precisely reproduce small-scale variations and extreme values in specific regions  
 315 and periods, it reasonably captures overall large-scale variations.

316



317

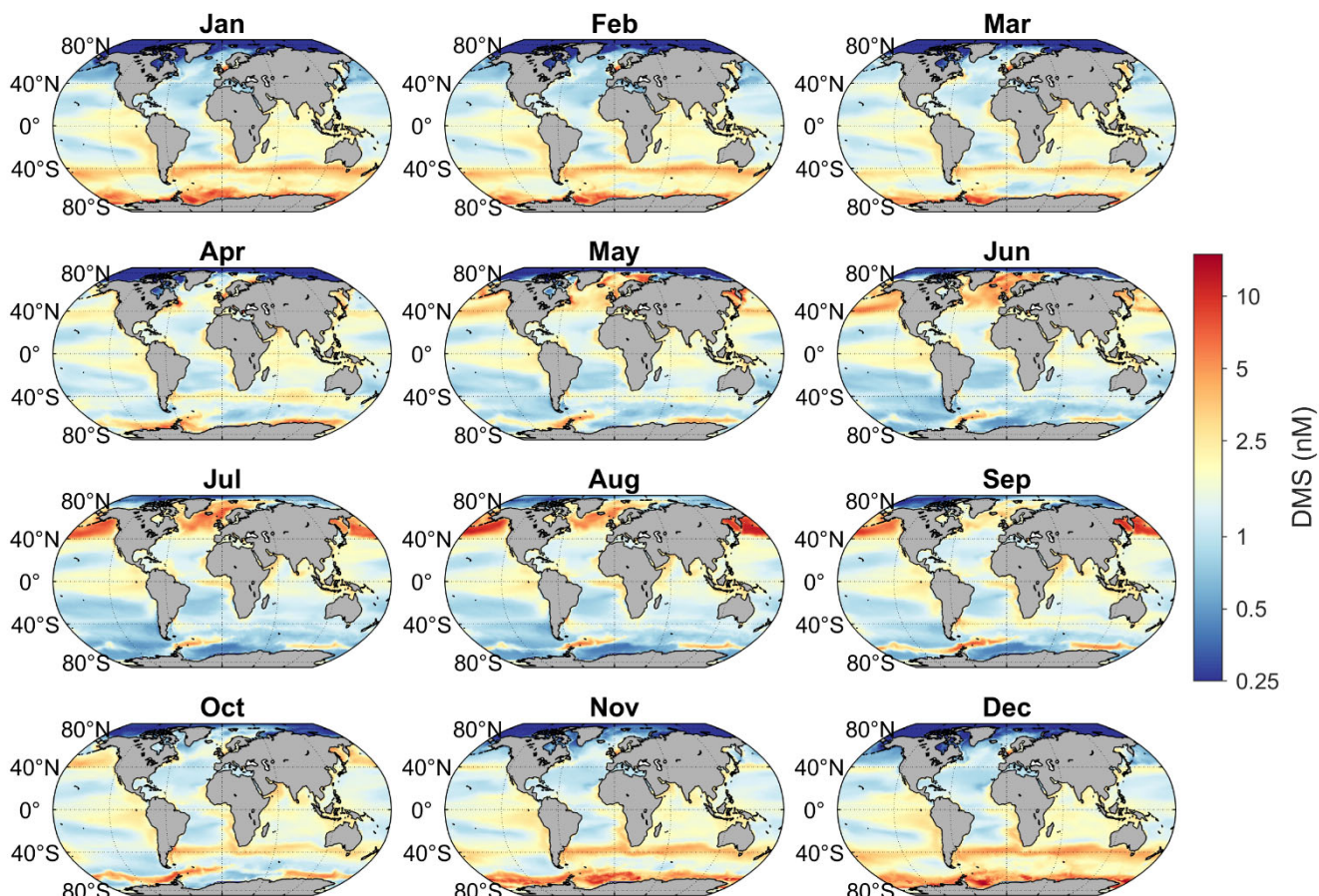
318 **Figure 5.** Comparisons between the ANN predictions and observations for fully independent campaigns. (a) Time series of  
 319 simulation results and DMS observational data obtained from *Line P Program*. The different markers represent different  
 320 stations of *Line P*. The blue shades cover the data obtained from the cruises included in the GSSD database but with a different  
 321 method. (b) Scatter plot of simulated versus observed DMS concentrations. (c) The same as panel b but for averaged data of  
 322 each cruise. The yellow lines and shaded bands are linear fittings and corresponding 95% confidence intervals for  $\log_{10}$  space  
 323 data. The values of  $R^2$ , RMSE, and slope displayed in the figure also correspond to  $\log_{10}$  space data.

324 **3.2 DMS distribution**325 **3.2.1 Spatial and seasonal variations**

326 The monthly climatology of ANN-simulated DMS concentrations in the global sea surface from 1998 to 2017 is shown in Fig.  
327 6. Overall, the DMS concentrations in mid- and high-latitude regions exhibit a significant seasonal cycle, peaking in summer  
328 and reaching their lowest in winter. This pattern aligns with the results of many prior observational studies. In the northern  
329 hemisphere, elevated DMS concentrations ( $> 2.5$  nM) during summer mainly occur in two regions. One is the North Pacific  
330 ( $40^{\circ}$ – $60^{\circ}$  N) where the concentration generally peaks in August, surpassing 10 nM (Fig. 6). The other is the subarctic North  
331 Atlantic ( $45^{\circ}$ – $80^{\circ}$  N). A notable increase of DMS concentration starts around  $45^{\circ}$ – $50^{\circ}$  N in May and gradually shifts northward  
332 beyond  $50^{\circ}$  N by July (Fig. 6–7). This spatiotemporal evolution pattern corresponds to the evolution of solar radiation intensity  
333 and the spring-summer bloom patterns of phytoplankton (Friedland et al., 2018; Yang et al., 2020). The peak concentration  
334 date at the same latitude in the North Atlantic generally precedes that in the North Pacific (Fig. 7). In the southern hemisphere,  
335 there is a conspicuous DMS-rich zone near  $40^{\circ}$  S (where the Subtropical Convergence lies) in summer, delineating a ring-  
336 shaped high-concentration band nearly parallel to the latitude. The highest seasonal mean concentration (December–February)  
337 occurs at  $41.5^{\circ}$  S, reaching 3.71 nM (Fig. 9). Southward from this zone, a low-DMS area spans  $47^{\circ}$ – $61^{\circ}$  S, where the average  
338 concentration is below 2.5 nM across all seasons. However, in the coastal waters of Antarctica (south of  $60^{\circ}$  S), significantly  
339 high concentrations also manifest in summer, surpassing 4.0 nM, even higher than those near  $40^{\circ}$  S (Fig. 6 and 9). In addition  
340 to the above regions, several typical upwelling zones also exhibit relatively higher DMS concentrations, such as the eastern  
341 Pacific and the Southeast Atlantic. The former, situated at lower latitudes, shows no significant seasonal variation, while the  
342 latter exhibits higher concentrations from October to February. The high nutrient concentrations in upwelling areas can bolster  
343 primary productivity, intensifying biological activities and augmenting the production of biogenic sulfur.

344

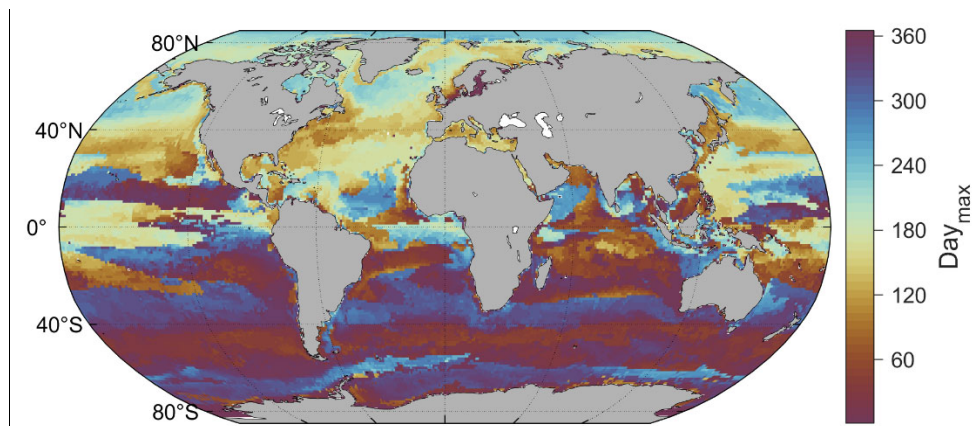
345



346

347 **Figure 6.** Monthly climatology of global sea surface DMS concentration during 1998 to 2017.

348



349

350 **Figure 7.** The day of the year with the highest sea surface DMS concentration for each grid point.

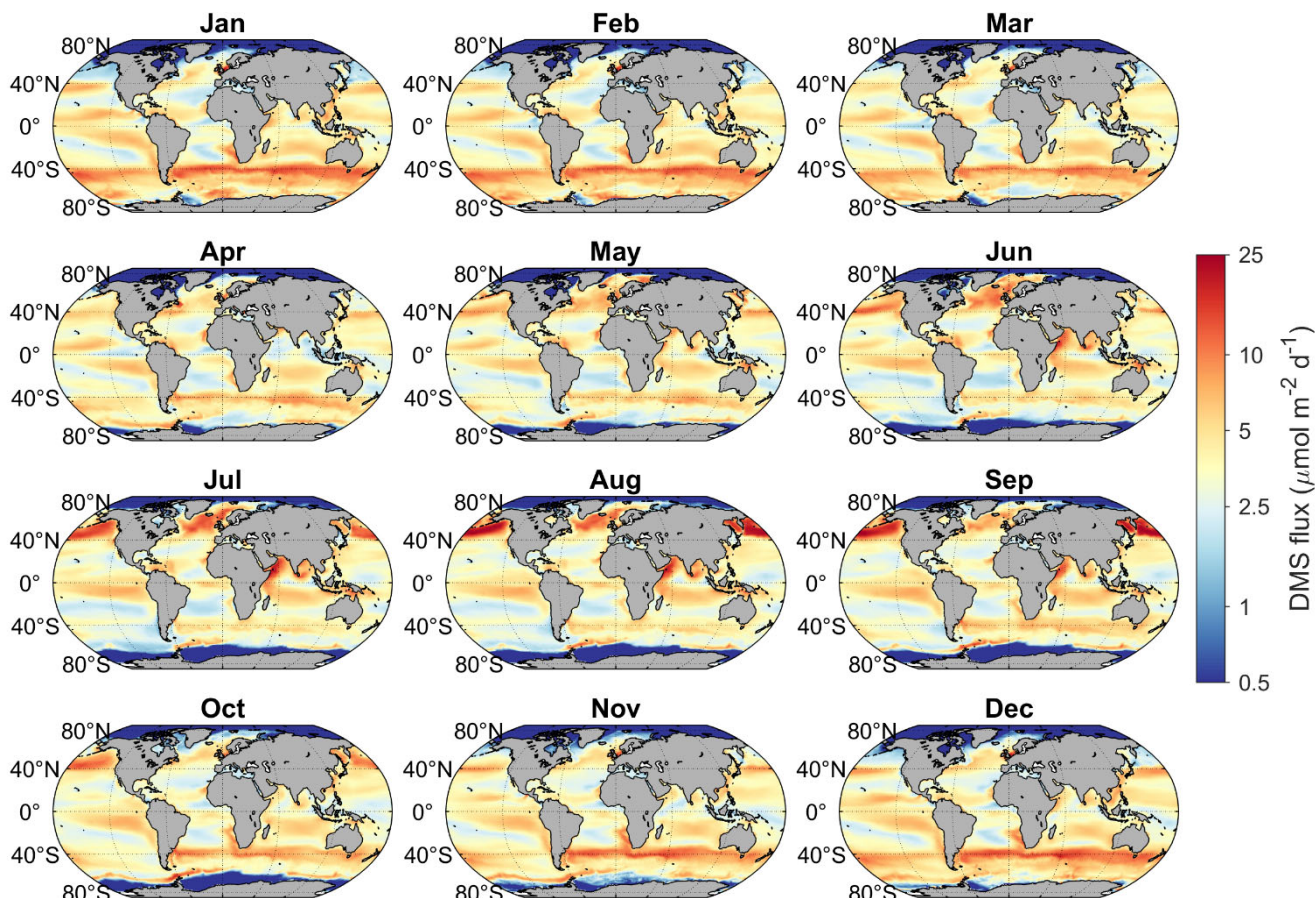
351

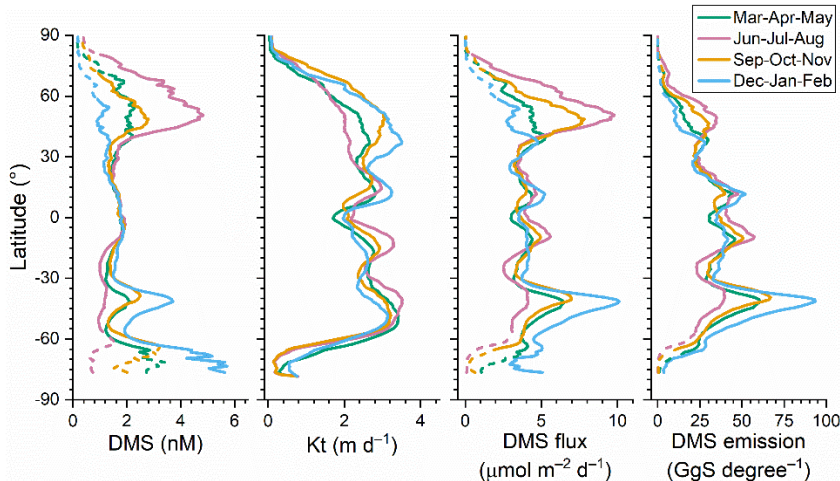
352 The spatiotemporal variation of DMS emission flux is generally consistent with that of concentration. As shown in Fig. 8,  
353 DMS fluxes are also significantly higher in summer across most mid- and high-latitude regions, and the high-flux regions  
354 generally overlap with the hot spots of DMS concentration. This indicates that the distribution of sea surface DMS  
355 concentration is the main factor controlling the monthly variation pattern of DMS emissions at the global scale, and the effect  
356 of transfer velocity is secondary. However, certain regions present inconsistencies between DMS flux and concentration  
357 dynamics. For instance, in the Arabian Sea and the central Indian Ocean, elevated transfer velocities (Fig. S10) during the June  
358 to September, driven by heightened wind speeds, markedly enhance emission fluxes, despite comparatively lower  
359 concentrations than other months. In polar regions, especially along the coast of Antarctica, although the DMS concentration  
360 is high in summer, sea ice coverage significantly impedes DMS release, thus the emission flux remains at a low level.

361 As shown in Fig. 9, the higher wind speeds in autumn and winter at mid- and high-latitudes result in higher total transfer  
362 velocities, leading to smaller summer-to-winter ratios of DMS emission flux compared to that of DMS concentration. In low  
363 latitudes, the existence of the trade wind zones in both hemispheres further leads to two high-flux bands. The emission fluxes  
364 in the equatorial region between these two trade zones are significantly lower. Although the latitudinal distributions of mean  
365 DMS emission fluxes in the southern and northern hemispheres are almost symmetrical, the huge difference in ocean area  
366 between the two hemispheres results in a significantly higher total emission from the southern hemisphere. Since  
367 anthropogenic SO<sub>2</sub> emissions are mainly concentrated in the northern hemisphere, oceanic DMS plays a much more important  
368 role in the southern hemisphere, especially over the regions south of 40° S where the DMS emission is high and the perturbation  
369 of anthropogenic pollution is low.

370 According to our newly built DMS gridded dataset, the global area-weighted annual mean concentration of DMS at the sea  
371 surface from 1998 to 2017 was ~1.71 nM (1.67–1.75 nM), which is within the range among the values (1.6 to 2.4 nM) obtained  
372 by various methods in previous studies (Tesdal et al., 2016). The global annual mean DMS emission to the atmosphere was  
373 17.2 TgS yr<sup>-1</sup> (16.9–17.5 TgS yr<sup>-1</sup>), with 10.3 TgS yr<sup>-1</sup> (59.9%) from the southern hemisphere and 6.9 TgS yr<sup>-1</sup> (40.1%) from  
374 the northern hemisphere.

375

378 **Figure 8.** Monthly climatology of global DMS sea-to-air flux from 1998 to 2017.



381  
382  
383  
384  
385

**Figure 9.** Latitudinal distributions of sea surface DMS concentration, total transfer velocity ( $K_t$ ), sea-to-air flux, and total emission in different seasons during 1998–2017. The dashed parts of the lines represent the missing ratio of satellite Chl  $a$  data for DMS simulation is higher than 0.5, thus most Chl  $a$  data is from CMEMS global biogeochemical multi-year hindcast.

### 386 3.2.2 Comparisons with other global DMS climatologies

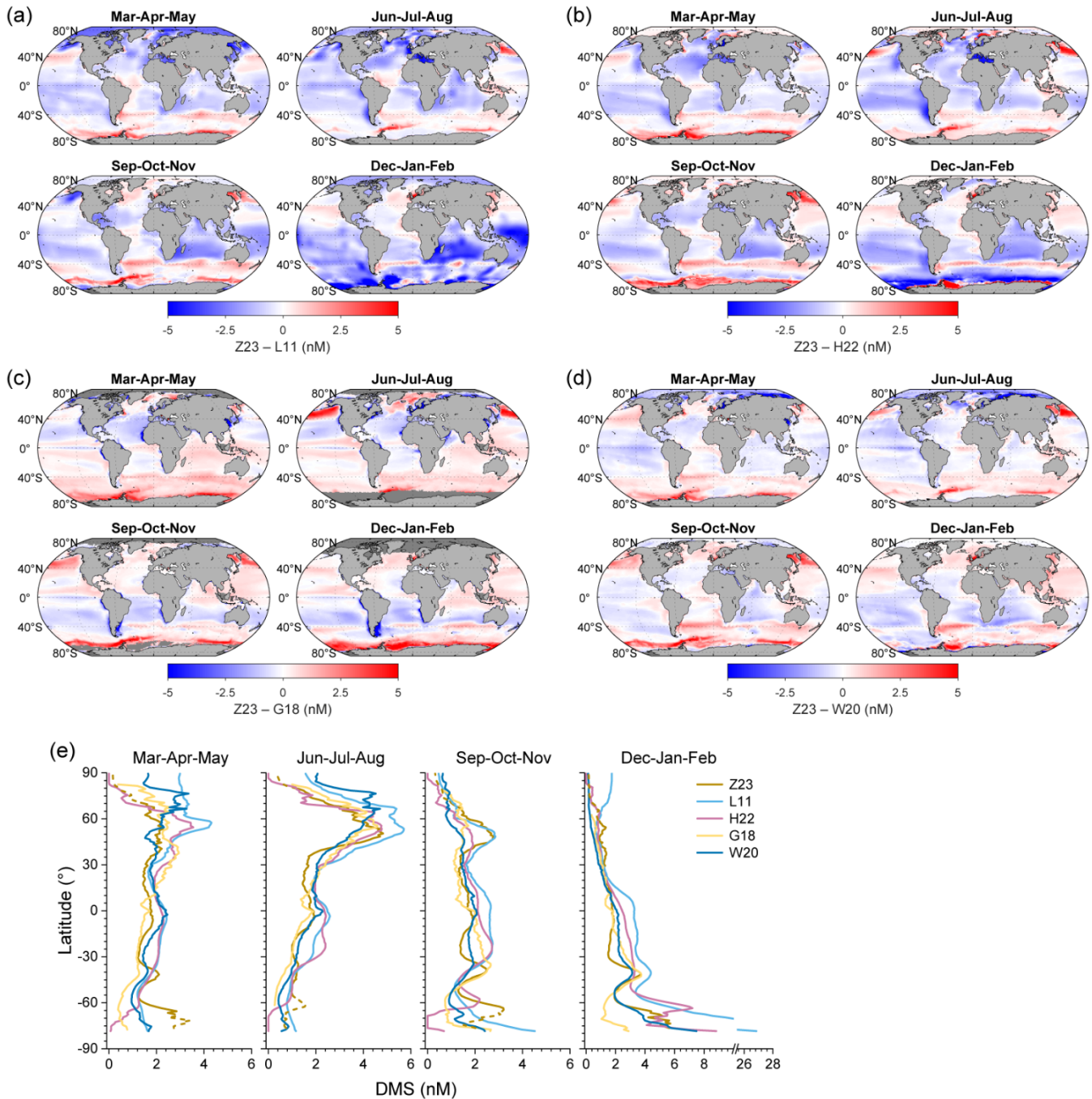
387 Here we compare the distributions of DMS concentration derived from our ANN simulation (referred to as Z23) with four  
388 previously constructed climatologies (Fig. 10), including (1) L11: the widely used second version of  
389 interpolation/extrapolation-based climatology established by Lana et al. (2011), (2) H22: an updated version of L11  
390 incorporating much more DMS measurements and using dynamic biogeochemical provinces (Hulswar et al., 2022), (3) G18:  
391 the DMS concentration field estimated by a two-step remote sensing algorithm (Galí et al., 2018), and (4) W20: the previous  
392 DMS climatology simulated by ANN (Wang et al., 2020).

393 Overall, all datasets exhibit the general pattern of high DMS concentration during summer and low concentration during winter,  
394 but notable distinctions emerge in their specific distributions. Due to the limitation of the method used,  $DMS_{L11}$  exhibits  
395 relatively lower spatial heterogeneity (i.e., higher patchiness), which may not well capture the detailed spatial variability on a  
396 regional scale. Compared with  $DMS_{L11}$ ,  $DMS_{Z23}$  is significantly lower at high latitudes during summer and in the South Indian  
397 Ocean and Southwest Pacific Ocean from December to February (Fig. 10a). Particularly in the southern polar region (Polar\_S),  
398 latitudinal averages of  $DMS_{L11}$  surpass 10 nM during summer, which are 1–3 times higher than  $DMS_{Z23}$  (Fig. 10e). However,  
399  $DMS_{Z23}$  maintains a similar level around the Antarctic in March compared to summer, and it is significantly higher than  
400  $DMS_{L11}$  as well as other three climatologies.  $DMS_{H22}$  shows lower disparities with  $DMS_{Z23}$  in the Arctic, the South Indian  
401 Ocean, and the Southwest Pacific Ocean, but the summertime concentrations in most of Polar\_S region are also > 2 nM higher  
402 than  $DMS_{Z23}$  (Fig. 10b). In contrast,  $DMS_{H22}$  in Polar\_S from September to November is ~2 nM lower than  $DMS_{Z23}$ . The

403 global area-weighted annual mean DMS concentrations in L11 and H22 are 2.43 nM and 2.26 nM, respectively, which are  
404 approximately 42.1% and 32.2% higher than Z23.

405 G18 exhibits the lowest global annual mean concentration (1.63 nM) among these climatologies, approximately 4.7% lower  
406 than Z23. The most notable deviation occurs in the North Pacific during boreal summer and near the Antarctic during austral  
407 summer, where  $DMS_{Z23}$  is  $> 3.5$  nM ( $> 100\%$ ) higher than  $DMS_{G18}$  (Fig. 10c). Conversely, there are high DMS concentrations  
408 ( $> 5$  nM) in certain coastal seas (such as the coasts of East and Northeast Asia, the coasts of Patagonia and Peru, the  
409 southwestern coast of Africa, and the western coasts of the Sahara Desert and North America) based on the G18 estimate. This  
410 characteristic is not fully replicated by other DMS fields, possibly due to the underestimation of DMS by our model and other  
411 methods in coastal regions as well as the overestimation of Chl  $a$  by satellites caused by the interference of colored dissolved  
412 organic matters and non-algal detrital particles (Aurin and Dierssen, 2012). W20 exhibits the highest consistency with Z23 in  
413 spatiotemporal distribution patterns as well as the lowest difference in global annual mean concentration (1.74 nM, only 1.8%  
414 higher than Z23). However, notable discrepancies exist in specific regions. For instance, during summertime,  $DMS_{Z23}$  is  $> 1$   
415 nM ( $> 40\%$ ) lower than  $DMS_{W20}$  in more than half of the Arctic area, while in North Pacific and Southern Ocean  $DMS_{Z23}$  is  
416 significantly higher than  $DMS_{W20}$  (Fig. 10d). Furthermore, only  $DMS_{Z23}$  forms a nearly complete high-concentration annular  
417 band at  $\sim 40^\circ$  S during austral summer.

418



421 **Figure 10.** (a-d) The spatial distributions of DMS concentration differences between Z23 and four previously estimated fields  
 422 across different seasons: (a) L11, (b) H22, (c) G18, and (d) W20. Dark gray regions in the ocean represent data missing in at  
 423 least one field. (e) Comparisons between the latitudinal distributions of Z23 and four previous DMS fields across different

424 seasons. The dashed parts of the Z23 lines represent the missing ratio of satellite Chl  $\alpha$  data for DMS simulation is higher than  
425 0.5, thus most Chl  $\alpha$  data is from CMEMS global biogeochemical multi-year hindcast.  
426

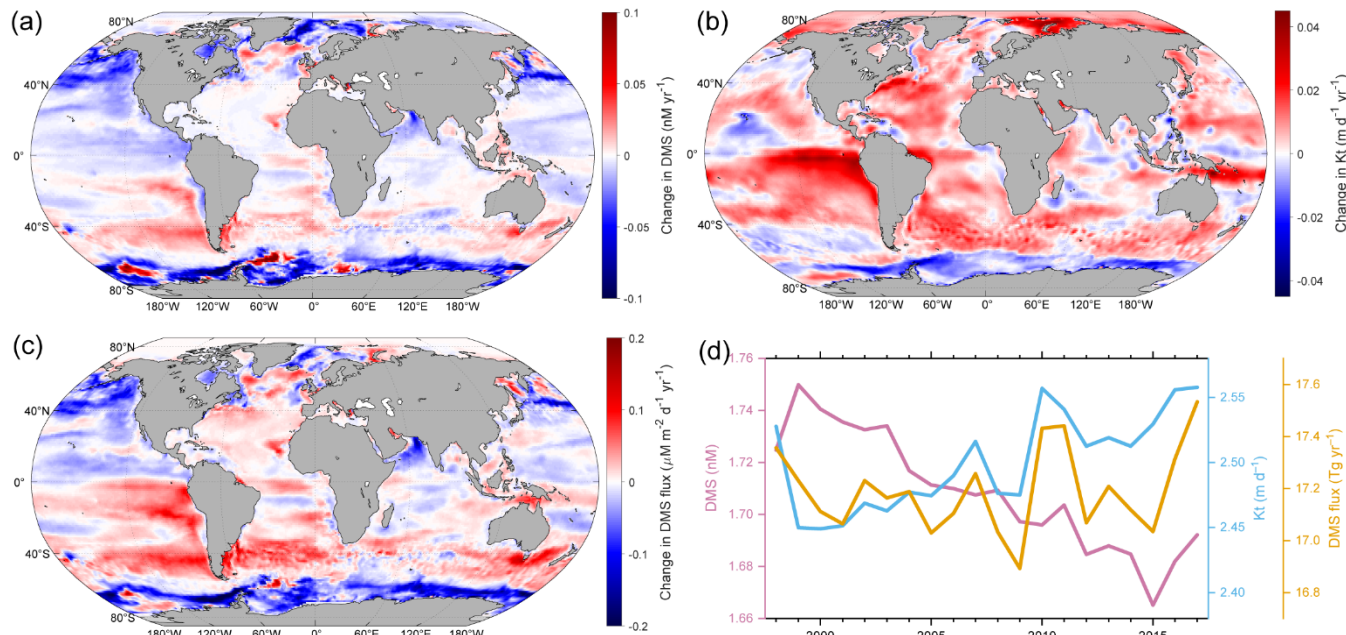
427 **3.2.3 Decadal changes**

428 One of the advantages of our ANN-derived DMS dataset is its time-resolved nature, which enables us to investigate the  
429 interannual variations in sea surface DMS concentration and flux. Here we present the decadal trends of DMS concentration,  
430  $K_t$ , and emission flux spanning from 1998 to 2017 at both global and regional scales. Overall, the absolute interannual  
431 variability of DMS concentration across most global oceanic regions appears relatively small. 88.4% of the global oceanic  
432 area exhibited a range of less than 1 nM between the maximum and minimum annual average concentrations during this 20-  
433 year period, particularly evident in tropical and subtropical regions with latitudes between 40° S and 40° N. At latitudes higher  
434 than 40° in both hemispheres, notable decadal changes occurred (Fig. 11a). Annual mean DMS concentrations in the Greenland  
435 Sea, the North Pacific, and the Southern Ocean exhibited significant decreasing trends with rates exceeding 0.03 nM yr<sup>-1</sup> ( $P <$   
436 0.05). A significant decreasing trend was also noted in the eastern tropical Pacific Ocean, albeit at a much lower absolute rate,  
437 primarily below 0.015 nM yr<sup>-1</sup>. Conversely, there were significant increasing trends in the Labrador Sea, the South Pacific  
438 (35° S – 60° S, 150° E – 75° W), and the southeastern Pacific, with the highest rate exceeding 0.02 nM yr<sup>-1</sup>. The global annual  
439 mean concentration exhibited a decreasing trend with a rate of 0.0035 nM yr<sup>-1</sup> ( $P < 0.05$ , Fig. 11d). The highest value (1.75  
440 nM) occurred in 1999, and the lowest concentration (1.67 nM) occurred in 2015. Due to the primary influences of increasing  
441 WS and secondary impact of rising SST in most mid- and low-latitude regions (Fig. S11), the  $K_t$  of DMS also showed an  
442 overall increasing trend, especially in the eastern Pacific and Atlantic Ocean (Fig. 11b). The increase in  $K_t$  can offset the  
443 decrease in DMS concentration to some extent, resulting in no significant trend in global DMS emissions during this 20-year  
444 period (Fig. 11d).

445 In the Arctic region, which stands as one of the most sensitive areas to climate warming (Screen et al., 2012; Serreze and  
446 Barry, 2011), the sea ice coverage has undergone significant reduction over the past two decades, particularly noticeable in the  
447 Barents Sea and Kara Sea, and further north ( $> 1\% \text{ yr}^{-1}$  for annual mean SI, Fig. S11). The retreat of summertime sea ice leads  
448 to an expansion of open-sea surface, potentially amplifying DMS emission (Galí et al., 2019). However, despite this trend,  
449 there was no significant increase in the annual total emission from the Polar\_N region over the same period, primarily due to  
450 a decreasing trend in DMS concentration (Fig. 12). On the other hand, the highest emission took place in the last two years ( $>$   
451 0.64 Tg yr<sup>-1</sup>), attributed to the highest  $K_t$ . Thus, it is likely that a rise in DMS emission will appear in future Arctic region with  
452 further loss of sea ice coverage (Galí et al., 2019). In contrast to the Arctic, the Southern Ocean has experienced a significant  
453 increase in sea ice fraction (Fig. S11), leading to a significant decrease in  $K_t$  (Fig. 11b). Coupled with the decreased DMS  
454 concentration, it resulted in a substantial decline in the DMS emission flux (Fig. 11c and 12). The highest annual total emission  
455 flux in the Polar\_S region occurred in 1998 (1.49 TgS), while the lowest occurred in 2013 (1.02 TgS), representing a decrease

456 of  $\sim 32\%$ . Across other oceanic regions, the annual average DMS concentrations in the Westerlies\_N\_Pacific and  
 457 Trades\_Pacific regions exhibit decreasing trends over the past 20 years, while the concentration in Westerlies\_S and  
 458 Trades\_Atlantic has increased ( $P < 0.05$ , Fig. 12). Regarding DMS flux, the Westerlies\_N\_Pacific showed a decrease, while  
 459 the Westerlies\_N\_Atlantic, Westerlies\_S, and Trades\_Atlantic showed an increase. There was no significant trend in other  
 460 low-latitude regions.

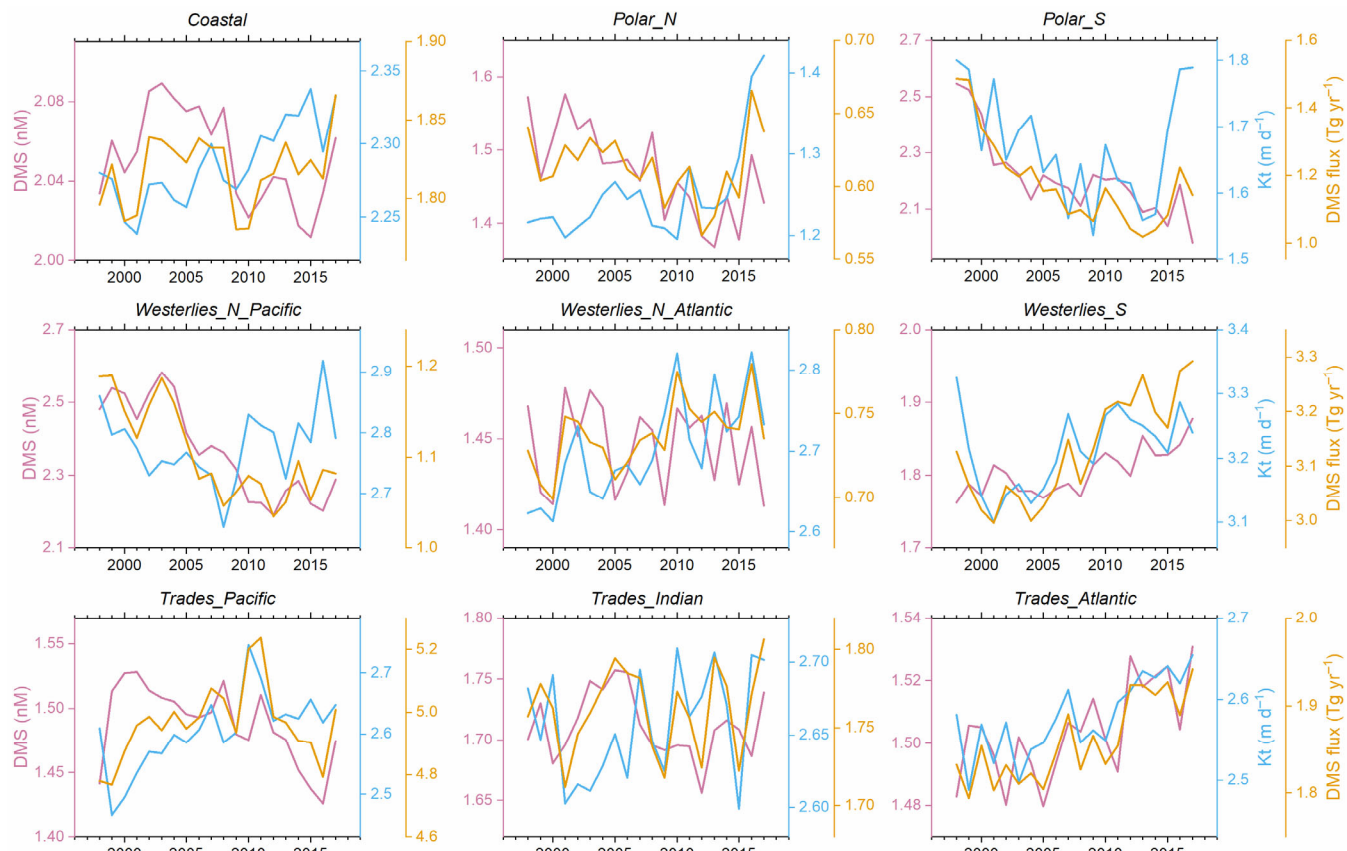
461



462

463 **Figure 11.** (a–c) The spatial distributions of changes in (a) DMS concentration, (b) Kt, and (c) DMS emission flux from 1998  
 464 to 2017. The linear regression slopes for the annual means are taken as the changing rates here. (d) The temporal changes of  
 465 global annual mean DMS concentration, Kt, and total emission flux from 1998 to 2017.

466



469 **Figure 12.** The temporal changes of annual mean DMS concentration, Kt, and total emission flux in different regions from  
 470 1998 to 2017.

### 471 3.3 Connection with atmospheric biogenic sulfur

472 One of the primary objectives of developing this daily gridded DMS dataset (Z23) spanning multiple years is to improve the  
 473 emission inventory of marine biogenic DMS, thereby enhancing the modelling performance for atmospheric sulfur chemistry,  
 474 especially for simulating sulfur-containing aerosols. To assess whether our newly constructed DMS dataset can reach this  
 475 objective, we employed a backward trajectory-based method to examine the correlation between sea surface DMS emissions  
 476 and resulting DMS oxidation products in the atmosphere. The correlation was then compared against those derived from  
 477 previously reported DMS climatologies (i.e., L11, H22, G18, and W20).

478 Here we use the observed concentrations of particulate methanesulfonic acid (MSA) over the Atlantic Ocean as a reference.  
 479 MSA is one of the major end-products of DMS in the atmosphere and is solely from the oxidation of marine biogenic DMS

480 over remote oceans (Saltzman et al., 1983; Savoie et al., 2002; Osman et al., 2019). Therefore, there is likely to be a dependence  
481 of the variation of MSA concentration on the DMS emission fluxes. During four transection cruises in the Atlantic conducted  
482 by *R/V Polarstern* (20 April – 20 May 2011, 28 October – 1 December 2011, 10 April – 15 May 2012, and 27 October – 27  
483 November 2012), the MSA concentrations in submicron aerosols were measured online using a High-Resolution Time-of-  
484 Flight Aerosol Mass Spectrometer. The ship tracks are shown in Fig. S12, and detailed information about the cruises and  
485 measurement methodology was provided by Huang et al. (2016). The 72-hour air mass backward trajectories reaching the ship  
486 position were calculated every hour by the HYSPLIT model, starting from a height of 100 m (Stein et al., 2015). Subsequently,  
487 the air mass exposure to DMS emission (AEDMS), denoting the weighted average of DMS emission flux along the trajectory  
488 path, was calculated following the approach of Zhou et al. (2021). We used 5 different DMS gridded datasets, including Z23,  
489 L11, H22, G18, and W20. For Z23, the calculated daily DMS fluxes were utilized. For the remaining 4 monthly climatologies,  
490 we applied the daily Kt data from Z23 to calculate the DMS fluxes, thus eliminating the potential confounding influences  
491 stemming from different Kt parameterizations. In this calculation, the same concentration was assigned to all days within a  
492 month without interpolation. Detailed procedures for the calculation of AEDMS are elucidated in Appendix C.

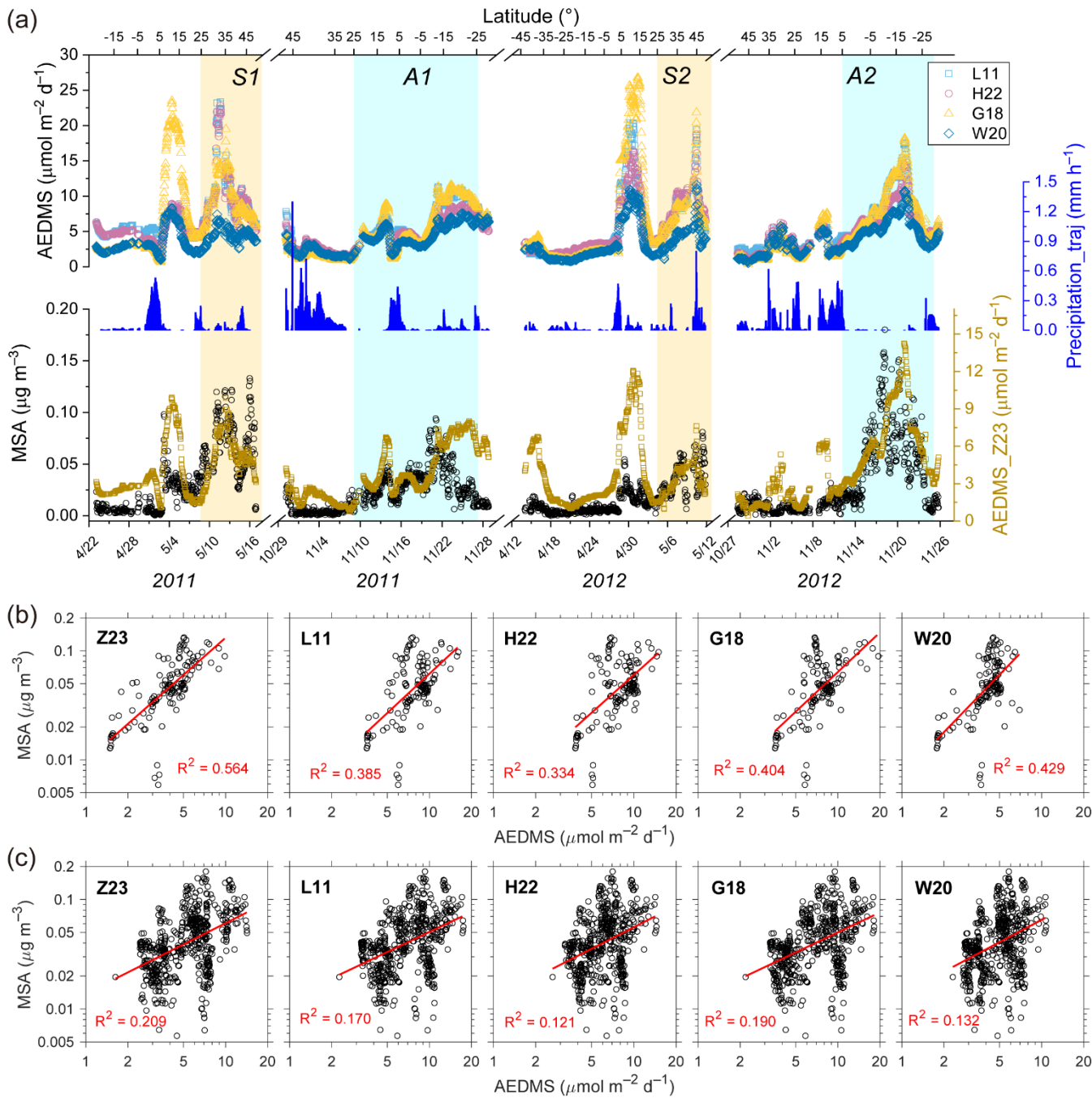
493 MSA concentrations were significantly higher in late spring than those in autumn for both North and South Atlantic Oceans  
494 (Fig. 13a). For example, during the boreal spring cruise in 2011, the average MSA concentration over the North Atlantic (0.068  
495  $\mu\text{g m}^{-3}$ , north of  $25^\circ \text{N}$ ) was about an order of magnitude higher than the average concentration over the South Atlantic (0.006  
496  $\mu\text{g m}^{-3}$ , south of  $5^\circ \text{S}$ ). During the boreal autumn cruise in 2011, the average concentration over the South Atlantic (0.034  $\mu\text{g}$   
497  $\text{m}^{-3}$ , south of  $5^\circ \text{S}$ ) was  $\sim$ 5 times higher than that over the North Atlantic (0.006  $\mu\text{g m}^{-3}$ , north of  $25^\circ \text{N}$ ). In addition to this  
498 major seasonal pattern, there was also a minor MSA concentration peak between  $5^\circ$ – $15^\circ \text{N}$  in both seasons. The spatial and  
499 seasonal variations of AEDMS based on the Z23 dataset (referred to as AEDMS\_Z23) largely coincided with these MSA  
500 concentration patterns (Fig. 13a). It should be noted that the MSA/AEDMS ratio between  $5^\circ$ – $15^\circ \text{N}$  was significantly lower  
501 than those in other high-MSA regions, which may result from the DMS simulation biases near the coast of West Africa or the  
502 lower DMS-to-MSA conversion yields related with air temperature and oxidant species (Barnes et al., 2006; Bates et al., 1992).  
503 There were also several AEDMS peaks in North Atlantic during November 2012, inconsistent with the continuously low MSA  
504 concentrations. Given the high precipitation rates along the trajectory (Fig. 13a), a strong wet scavenging process might  
505 significantly reduce aerosol concentrations (Wood et al., 2017).

506 The AEDMS derived from other DMS concentration fields showed similar variations to AEDMS\_Z23 (Fig. 13a). It is not  
507 surprising since all DMS concentration fields exhibit similar large-scale spatiotemporal patterns, and identical air mass  
508 transport path and Kt were applied in different AEDMS calculations. However, due to the lower temporal resolutions and  
509 absence of interannual changes in those DMS monthly climatologies, the resulting AEDMS may be less effective in capturing  
510 variability at finer scales or across different years. Here we focus on the high-MSA periods to elaborate on this issue, which  
511 corresponds to latitudes north of  $25^\circ \text{N}$  in boreal spring (S1 and S2 in Fig. 13a),  $25^\circ \text{N}$  –  $25^\circ \text{S}$  in boreal autumn of 2011 (A1

512 in Fig. 13a), and south of 5° N in boreal autumn of 2012 (A2 in Fig. 13a). As shown in Fig. 13b, hourly MSA concentrations  
513 exhibited significantly stronger correlations with AEDMS\_Z23 than with other AEDMS time series in S1 and S2, indicating  
514 AEDMS\_Z23 can explain more (1.31 – 1.69 times) variance of MSA concentration. During A1 and A2, the correlations  
515 between AEDMS and MSA concentration were weaker than those during S1 and S2, possibly due to higher DMS prediction  
516 biases in South Atlantic or different influencing factors on atmospheric DMS chemistry across wide spatial ranges.  
517 Nonetheless, AEDMS\_Z23 still exhibited the highest correlation with MSA (Fig. 13c). This overall stronger connection  
518 between Z23 and atmospheric DMS-derived aerosols mainly benefited from the combined effects of higher time resolution  
519 and inherent interannual variations. For example, the ratio of average MSA concentration during S1 to that during S2 (S1-to-  
520 S2 ratio) was 1.89, and the A2-to-A1 ratio was 1.75. AEDMS\_Z23 exhibited a slightly lower but still significant interannual  
521 variation degree, where the S1-to-S2 ratio and A2-to-A1 ratio were 1.58 and 1.46, respectively. However, this interannual  
522 variation cannot be reproduced by other datasets, where the S1-to-S2 ratio and A2-to-A1 ratio were in the range of 1.08–1.30  
523 and 1.19–1.29, respectively. These results manifest the potential of our newly developed DMS gridded data product to enhance  
524 the modeling performance for atmospheric DMS processes compared with previously reported climatologies.

525 It is worth noting that the satellite-based algorithms of G18 and ANN model of W20 can also be utilized to produce daily  
526 multiyear DMS fields as Z23. Future investigations could include comparisons with these fields, facilitating a more  
527 comprehensive assessment of the performance of each algorithm/model. Furthermore, the AEDMS method used here is a  
528 highly simplified approach without considering the complex DMS chemistry in the atmosphere, and the intercomparisons  
529 based on chemical transport models can be used in the future to obtain a more straightforward conclusion.

530



531

532 **Figure 13.** (a) Time series of observed MSA concentration, AEDMS calculated based on different DMS concentration  
 533 datasets, and average precipitation along the backward trajectory (Precipitation\_traj) during four Atlantic cruises in 2011–  
 534 2012. (b–c) Correlations between hourly MSA concentration and AEDMS based on different DMS concentration datasets (b)

535 during periods S1 + S2 and (c) during periods A1 + A2. Data points during the periods with air mass time fraction within the  
536 boundary layer less than 90% or Precipitation\_traj larger than 0.05 mm h<sup>-1</sup> were removed.

537 **4 Uncertainties and limitations**

538 Although our ANN ensemble model and derived DMS dataset demonstrate certain advantages compared to previous studies,  
539 as discussed in Section 3.3, there persist notable uncertainties and limitations, which result in the ~35% uncaptured variance  
540 (Fig. 3a) and non-negligible simulation biases, e.g., underestimation of extremely high DMS concentrations and overestimation  
541 of low DMS concentrations. Firstly, there is a mismatch in the spatial and temporal scales between the input and target. The  
542 target, sea surface DMS concentrations, are obtained from in-situ measurements taken at specific locations and time points. In  
543 contrast, the input data are primarily from gridded datasets where each pixel represents an average over a defined spatial and  
544 temporal range. This is particularly significant for the ECCO variables, which have the largest spatial grid size of 110 km.  
545 Consequently, extreme values at specific locations cannot be accurately captured by the regional averages, resulting in  
546 damped variations among the samples. Secondly, the input data from different sources and the observed sea surface DMS  
547 concentrations inherently possess certain uncertainties, which can introduce noises into the ANN learning process. Thirdly,  
548 the ANN itself may not be powerful enough to fully capture the complex input-output relationships across different oceanic  
549 regions, especially when the samples are scarce under specific environmental conditions. Finally, beyond the 9 variables  
550 incorporated in this study, other environmental parameters such as pH (Six et al., 2013; Hopkins et al., 2010) and trace metal  
551 elements (Li et al., 2021) can also influence DMS concentration. Not incorporating these factors may introduce additional  
552 biases.

553 The overall bias for  $\log_{10}\text{DMS}$  is at a similar level between high- and low-concentration ends, but the DMS concentration on  
554 a linear scale is more underestimated in the high-concentration regime than it is overestimated in the low-concentration regime.  
555 As a result, our simulation results may tend to underestimate the annual average DMS concentration and flux. To mitigate this  
556 critical bias and reduce model uncertainty, high-quality input datasets with finer spatial resolution are needed in the future.  
557 The high-time resolution nature of the resulted daily DMS data product would be more valuable if accompanied by higher  
558 spatial resolution. Expanding the data volume is also crucial for improving model performance. Although the current DMS  
559 observational data covers all major oceanic basins, certain regions such as the Trades\_Pacific remain underrepresented.  
560 Advances in online measurement technologies offer promising avenues for acquiring more extensive and convenient  
561 observational data (Hulswar et al., 2022). Additionally, incorporating more input features to the model would be beneficial.  
562 This necessitates a comprehensive understanding of the spatiotemporal distributions of those input features, and further field  
563 measurements are important to this end. Moreover, integrating DMS biogeochemical mechanisms with machine learning  
564 technique, i.e., a hybrid model coupling physical processes with data-driven approach, may further improve prediction  
565 accuracy, generalization, and interpretability (Reichstein et al., 2019).

566 When using our newly developed DMS dataset, there are two issues that need to be noted. Firstly, there is a significant portion  
567 of missing satellite Chl  $\alpha$  data during winter in polar regions. In such instances, the modeling data from CMEMS global  
568 biogeochemical multi-year hindcast was used, which may introduce higher uncertainty. We have provided the flags indicating  
569 the source of Chl  $\alpha$  data for each grid in the dataset. Nevertheless, given the low phytoplankton biomass and extensive sea ice  
570 coverage during winter, DMS emissions are typically at the lowest level of the year, thus the satellite data missing has a  
571 relatively small impact on investigating the subsequent effects of DMS emission on atmospheric environment. Secondly, since  
572 the ANN ensemble model exhibits limited capacity in accurately reproducing extremely high concentrations of DMS, the DMS  
573 concentrations in certain nearshore areas with intensive biological activity may be greatly underestimated.

## 574 **5 Code and data availability**

575 The generated gridded datasets of DMS concentration, total transfer velocity, and flux have been deposited at  
576 <https://doi.org/10.5281/zenodo.1187990> (Zhou et al., 2024) and can be downloaded publicly. The ANN model code and the  
577 Matlab scripts for data analysis are available from <https://doi.org/10.5281/zenodo.12398985> (Zhou, 2024).

## 578 **6 Conclusion**

579 Based on the global sea surface DMS observations and associated data of 9 relevant environmental variables, an ANN  
580 ensemble model was trained. The ANN model effectively captures the variability of DMS concentrations and demonstrates  
581 good simulation accuracy. Leveraging this ANN model, a global sea surface DMS gridded dataset with a daily resolution  
582 spanning 20 years (1998–2017) was constructed. The global annual average concentration was  $\sim$ 1.71 nM, falling within the  
583 range of previous estimates, and the annual total emission was  $\sim$ 17.2 TgS yr $^{-1}$ . High DMS concentrations and fluxes took place  
584 during summer in North Pacific (40°–60° N), North Atlantic (50°–80° N), the annular band around 40° S, and the Southern  
585 Ocean. With this newly developed dataset, the day-to-day changes and interannual variations can be investigated. The global  
586 annual average concentration shows a mild decreasing trend ( $\sim$ 0.0035 nM yr $^{-1}$ ), while the total emission remains stable. There  
587 were more significant decadal changes in certain regions. Specifically, the annual DMS emission in the South Pacific and  
588 North Pacific showed opposite trends.

589 To further validate the robustness and advantages of our new dataset, an airmass trajectory-based approach was applied to link  
590 the DMS flux and atmospheric MSA concentration. Compared to previous monthly climatologies, the airmass exposure to  
591 DMS calculated using our new dataset explains a greater amount of variance in atmospheric MSA concentration over the  
592 Atlantic Ocean. Therefore, despite the presence of uncertainties and limitations, the new dataset holds the potential to serve as  
593 an improved DMS emission inventory for atmospheric models and enhance the simulation of DMS-induced aerosols and their  
594 associated climatic effects.

595

596 **Appendix A: Acronyms**

597	AEDMS	Air mass exposure to DMS emission
598	ANN	Artificial neural network
599	BLH	Boundary layer height
600	CCN	Cloud condensation nuclei
601	Chl <i>a</i>	Chlorophyll <i>a</i>
602	DMS	Dimethyl sulfide
603	DMSP	Dimethylsulfoniopropionate
604	DO	Dissolved oxygen
605	DSWF	Downward short-wave radiation flux
606	ECCO	Estimating the Circulation and Climate of the Ocean
607	GSSD database	Global Surface Seawater DMS database
608	K <sub>t</sub>	Total transfer velocity
609	MLD	Mixed layer depth
610	MB	Mean bias
611	MSA	Methanesulfonic acid
612	MSE	Mean square error
613	NAAMES	North Atlantic Aerosols and Marine Ecosystems Study
614	NMB	Normalized mean bias
615	RMSE	Rooted mean square error
616	SI	Sea ice fraction
617	SST	Sea surface temperature
618	SSS	Sea surface salinity
619	WS	Wind speed

620

621 **Appendix B: The weighted resampling strategy**

622 Apart from the data imbalance between coastal and non-coastal regions, there exists an imbalance across different DMS  
623 concentration ranges. The majority of DMS concentrations (78.6%) fall within the range of 0.8 to 10 nM ( $\log_{10}(\text{DMS})$  between  
624 -0.1 to 1). Samples with DMS concentrations exceeding 15 nM or falling below 0.3 nM only represent 6.9% of the entire  
625 sample set. A weighted resampling strategy was applied to mitigate this imbalance (Fig. S7). We randomly sampled 50,000  
626 samples with replacement from the original sample set. The probability of each sample being selected is proportional to the  
627 weighting factor shown as the red dash line in Fig. S7b, which is dependent on its DMS concentration. First, the probability  
628 distribution of initial  $\log_{10}(\text{DMS})$  values was fitted with a gamma distribution, which is given below and displayed as the blue  
629 line in Fig. S7b:

630 
$$f(x) = \frac{1}{\Gamma(k)\theta^k} (x + 4)^{k-1} e^{-(x+4)/\theta} \quad (A1)$$

631 Here  $k$  and  $\theta$  represent the shape parameter and scale parameter, in this case, 100.7 and 0.044, respectively.  $x$  is the  $\log_{10}(\text{DMS})$   
 632 value. Since gamma distribution only takes positive values, we added 4 to the original  $x$  as the dependent variable for  
 633 distribution fitting. We then obtained a new gamma distribution function with the same mode but lower shape parameter, in  
 634 which  $k = 40$  and  $\theta = 0.112$ . The reciprocal of the new gamma distribution function was taken as the weighting factor. As a  
 635 result, samples exhibiting high or low DMS concentrations are more likely to be selected, whereas those with intermediate  
 636 concentrations are less likely to be selected. We also controlled the  $F_{\text{coastal}}$  value of the resampled data equal to 9.7%. The data  
 637 distribution of DMS concentrations after the resampling process is shown in Fig. S7c. The fraction of samples with DMS  
 638 concentrations above 15 nM or below 0.3 nM is elevated to 15.0%. The 50,000 samples were then randomly split to a training  
 639 set (80%) and a validation set (20%). Since there are duplicate samples in the resampled dataset, the random data split was  
 640 conducted based on the original sample ID before resampling to ensure that there was no sample overlap between the training  
 641 and validation sets.

642

#### 643 **Appendix C: The calculation of airmass exposure to DMS emission (AEDMS)**

644 Here the AEDMS index followed the similar calculation of the air mass exposure to Chl  $a$  (AEC) in previous studies (Arnold  
 645 et al., 2010; Park et al., 2018; Zhou et al., 2021). We adopted the similar approach presented in Zhou et al. (2021) by replacing  
 646 the Chl  $a$  concentration with DMS flux, as shown in the following equation (A2):

647 
$$AEDMS = \frac{\sum_{i=0}^{72} DMS\ flux_i e^{-\frac{t_i}{72} \frac{500}{BLH}}}{\sum_{i=0}^{72} e^{-\frac{t_i}{72}}} \quad (A2)$$

648 Here  $i$  represents the  $i$ -th trajectory point of the 72-hour backward trajectory (0-th for the receptor point).  $DMS\ flux_i$  represents  
 649 the DMS flux of the pixel where the  $i$ -th trajectory point locates.  $DMS\ flux_i$  is set to zero if the point locates on land or the  
 650 air mass pressure is below 850 hPa (usually in the free troposphere with little influence of surface emission).  $t_i$  is the tracking  
 651 time of the trajectory point (unit: hour) and  $e^{-\frac{t_i}{72}}$  is the weighting factor to assign higher values for regions closer to the receptor  
 652 point. To better connect with the atmospheric concentrations in the marine boundary layer, the normalization by boundary  
 653 layer height (BLH) is added by the  $\frac{500}{BLH}$  term. The BLH below 50 m is replaced by 50 m.

654 **Author contributions.**

655 SZ and YC designed the research. SZ, FW, ZX, and KY collected the data and did the data preprocessing. SZ implemented  
 656 the model development and performed the simulation with assistance from GY, HZ, and YZ. SH, HH, AW, and LP provided  
 657 the measurement data of atmospheric MSA over the Atlantic Ocean. SZ conducted the data analysis and visualization with  
 658 advice from YC and XG. SZ and YC wrote the manuscript with inputs from all authors.

659 **Competing interests.**

660 The authors declare that they have no conflict of interest.

661 **Acknowledgements.**

662 We greatly thank National Oceanic and Atmospheric Administration's Pacific Marine Environmental Laboratory for  
663 maintaining the Global Surface Seawater DMS Database. We acknowledge Dr. Martin Johnson for sharing the code of DMS  
664 transfer velocity calculation. We also thank Dr. Rich Pawlowicz for developing and sharing the M\_Map toolbox for Matlab  
665 (<https://www.eoas.ubc.ca/~rich/map.html>), which was used in the mapping of this study. XG was supported by the Research  
666 Center for Industries of the Future (RCIF) at Westlake University and Westlake University Education Foundation.

667 **Financial support.**

668 This work is jointly supported by Natural Science Foundation of Shanghai (22ZR1403800), National Key Research and  
669 Development Program of China (2016YFA0601304), and National Natural Science Foundation of China (41775145).

670

671 **References**

- 672 Abdar, M., Pourpanah, F., Hussain, S., Rezazadegan, D., Liu, L., Ghavamzadeh, M., Fieguth, P., Cao, X., Khosravi, A.,  
673 Acharya, U. R., Makarenkov, V., and Nahavandi, S.: A review of uncertainty quantification in deep learning: Techniques,  
674 applications and challenges, *Information Fusion*, 76, 243-297, 10.1016/j.inffus.2021.05.008, 2021.
- 675 Alcolombri, U., Ben-Dor, S., Feldmesser, E., Levin, Y., Tawfik, D. S., and Vardi, A.: Identification of the algal dimethyl  
676 sulfide-releasing enzyme: a missing link in the marine sulfur cycle, *Science*, 348, 1466-1469, 2015.
- 677 Andreae, M. O.: Ocean-Atmosphere Interactions in the Global Biogeochemical Sulfur Cycle, *Mar. Chem.*, 30, 1-29, Doi  
678 10.1016/0304-4203(90)90059-L, 1990.
- 679 Arnold, S. R., Spracklen, D. V., Gebhardt, S., Custer, T., Williams, J., Peeken, I., and Alvain, S.: Relationships between  
680 atmospheric organic compounds and air-mass exposure to marine biology, *Environ. Chem.*, 7, 232-241, 10.1071/en09144,  
681 2010.
- 682 Aurin, D. A., and Dierssen, H. M.: Advantages and limitations of ocean color remote sensing in CDOM-dominated, mineral-  
683 rich coastal and estuarine waters, *Remote Sensing of Environment*, 125, 181-197, 10.1016/j.rse.2012.07.001, 2012.
- 684 Barnes, I., Hjorth, J., and Mihalopoulos, N.: Dimethyl sulfide and dimethyl sulfoxide and their oxidation in the atmosphere,  
685 *Chem. Rev.*, 106, 940-975, 10.1021/cr020529+, 2006.

- 686 Bates, T. S., Calhoun, J. A., and Quinn, P. K.: Variations in the Methanesulfonate to Sulfate Molar Ratio in Submicrometer  
687 Marine Aerosol-Particles over the South-Pacific Ocean, *J. Geophys. Res.-Atmos.*, 97, 9859-9865, 10.1029/92JD00411, 1992.
- 688 Beale, R., Johnson, M., Liss, P. S., and Nightingale, P. D.: Air-Sea Exchange of Marine Trace Gases, in: *Treatise on*  
689 *Geochemistry (Second Edition)*, edited by: Holland, H. D., and Turekian, K. K., 2, Elsevier, Oxford, 53-92, 2014.
- 690 Behrenfeld, M. J., Moore, R. H., Hostetler, C. A., Graff, J., Gaube, P., Russell, L. M., Chen, G., Doney, S. C., Giovannoni, S.,  
691 Liu, H., Proctor, C., Bolaños, L. M., Baetge, N., Davie-Martin, C., Westberry, T. K., Bates, T. S., Bell, T. G., Bidle, K. D.,  
692 Boss, E. S., Brooks, S. D., Cairns, B., Carlson, C., Halsey, K., Harvey, E. L., Hu, C., Karp-Boss, L., Kleb, M., Menden-Deuer,  
693 S., Morison, F., Quinn, P. K., Scarino, A. J., Anderson, B., Chowdhary, J., Crosbie, E., Ferrare, R., Hair, J. W., Hu, Y., Janz,  
694 S., Redemann, J., Saltzman, E., Shook, M., Siegel, D. A., Wisthaler, A., Martin, M. Y., and Ziembka, L.: The North Atlantic  
695 Aerosol and Marine Ecosystem Study (NAAMES): Science Motive and Mission Overview, *Front. Mar. Sci.*, 6,  
696 10.3389/fmars.2019.00122, 2019.
- 697 Bell, T. G., Porter, J. G., Wang, W.-L., Lawler, M. J., Boss, E., Behrenfeld, M. J., and Saltzman, E. S.: Predictability of  
698 Seawater DMS During the North Atlantic Aerosol and Marine Ecosystem Study (NAAMES), *Front. Mar. Sci.*, 7, 596763,  
699 10.3389/fmars.2020.596763, 2021.
- 700 Belviso, S., Bopp, L., Moulin, C., Orr, J. C., Anderson, T. R., Aumont, O., Chu, S., Elliott, S., Maltrud, M. E., and Simó, R.:  
701 Comparison of global climatological maps of sea surface dimethyl sulfide, *Glob. Biogeochem. Cycles*, 18,  
702 10.1029/2003gb002193, 2004a.
- 703 Belviso, S., Moulin, C., Bopp, L., and Stefels, J.: Assessment of a global climatology of oceanic dimethylsulfide (DMS)  
704 concentrations based on SeaWiFS imagery (1998-2001), *Canadian Journal of Fisheries and Aquatic Sciences*, 61, 804-816,  
705 10.1139/f04-001, 2004b.
- 706 Belviso, S., Masotti, I., Tagliabue, A., Bopp, L., Brockmann, P., Fichot, C., Caniaux, G., Prieur, L., Ras, J., Uitz, J., Loisel,  
707 H., Dessailly, D., Alvain, S., Kasamatsu, N., and Fukuchi, M.: DMS dynamics in the most oligotrophic subtropical zones of  
708 the global ocean, *Biogeochemistry*, 110, 215-241, 10.1007/s10533-011-9648-1, 2011.
- 709 Bergen, K. J., Johnson, P. A., de Hoop, M. V., and Beroza, G. C.: Machine learning for data-driven discovery in solid Earth  
710 geoscience, *Science*, 363, eaau0323, 10.1126/science.aau0323, 2019.
- 711 Carslaw, K. S., Lee, L. A., Reddington, C. L., Pringle, K. J., Rap, A., Forster, P. M., Mann, G. W., Spracklen, D. V.,  
712 Woodhouse, M. T., Regayre, L. A., and Pierce, J. R.: Large contribution of natural aerosols to uncertainty in indirect forcing,  
713 *Nature*, 503, 67-71, 10.1038/nature12674, 2013.
- 714 Charlson, R. J., Lovelock, J. E., Andreae, M. O., and Warren, S. G.: Oceanic phytoplankton, atmospheric sulphur, cloud  
715 albedo and climate, *Nature*, 326, 655-661, 10.1038/326655a0, 1987.
- 716 Chawla, N. V., Bowyer, K. W., Hall, L. O., and Kegelmeyer, W. P.: SMOTE: synthetic minority over-sampling technique,  
717 *Journal of artificial intelligence research*, 16, 321-357, 2002.

- 718 Chen, Q., Sherwen, T., Evans, M., and Alexander, B.: DMS oxidation and sulfur aerosol formation in the marine troposphere:  
719 a focus on reactive halogen and multiphase chemistry, *Atmos. Chem. Phys.*, 18, 13617-13637, 10.5194/acp-18-13617-2018,  
720 2018.
- 721 Dubitzky, W., Granzow, M., and Berrar, D. P.: *Fundamentals of data mining in genomics and proteomics*, Springer Science  
722 & Business Media, 2007.
- 723 Forget, G., Campin, J.-M., Heimbach, P., Hill, C. N., Ponte, R. M., and Wunsch, C.: ECCO version 4: An integrated framework  
724 for non-linear inverse modeling and global ocean state estimation, *Geosci. Model Dev.*, 8, 3071-3104, 2015.
- 725 Friedland, K. D., Mouw, C. B., Asch, R. G., Ferreira, A. S. A., Henson, S., Hyde, K. J. W., Morse, R. E., Thomas, A. C., and  
726 Brady, D. C.: Phenology and time series trends of the dominant seasonal phytoplankton bloom across global scales, *Global  
727 Ecology and Biogeography*, 27, 551-569, 10.1111/geb.12717, 2018.
- 728 Fung, K. M., Heald, C. L., Kroll, J. H., Wang, S., Jo, D. S., Gettelman, A., Lu, Z., Liu, X., Zaveri, R. A., Apel, E. C., Blake,  
729 D. R., Jimenez, J. L., Campuzano-Jost, P., Veres, P. R., Bates, T. S., Shilling, J. E., and Zawadowicz, M.: Exploring dimethyl  
730 sulfide (DMS) oxidation and implications for global aerosol radiative forcing, *Atmos. Chem. Phys.*, 22, 1549-1573,  
731 10.5194/acp-22-1549-2022, 2022.
- 732 Galí, M., Devred, E., Levasseur, M., Royer, S.-J., and Babin, M.: A remote sensing algorithm for planktonic  
733 dimethylsulfoniopropionate (DMSP) and an analysis of global patterns, *Remote Sensing of Environment*, 171, 171-184,  
734 10.1016/j.rse.2015.10.012, 2015.
- 735 Galí, M., and Simó, R.: A meta-analysis of oceanic DMS and DMSP cycling processes: Disentangling the summer paradox,  
736 *Glob. Biogeochem. Cycles*, 29, 496-515, 10.1002/2014gb004940, 2015.
- 737 Galí, M., Levasseur, M., Devred, E., Simó, R., and Babin, M.: Sea-surface dimethylsulfide (DMS) concentration from satellite  
738 data at global and regional scales, *Biogeosciences*, 15, 3497-3519, 10.5194/bg-15-3497-2018, 2018.
- 739 Galí, M., Devred, E., Babin, M., and Levasseur, M.: Decadal increase in Arctic dimethylsulfide emission, *P. Natl. Acad. Sci.  
740 USA*, 116, 19311-19317, 10.1073/pnas.1904378116, 2019.
- 741 Garnesson, P., Mangin, A., Fanton d'Andon, O., Demaria, J., and Bretagnon, M.: The CMEMS GlobColour chlorophyll a  
742 product based on satellite observation: Multi-sensor merging and flagging strategies, *Ocean Science*, 15, 819-830, 2019.
- 743 Haibo, H., Yang, B., Garcia, E. A., and Shutao, L.: ADASYN: Adaptive synthetic sampling approach for imbalanced learning,  
744 2008 IEEE International Joint Conference on Neural Networks (IEEE World Congress on Computational Intelligence), 2008,  
745 1322-1328.
- 746 Hoffmann, E. H., Tilgner, A., Schroedner, R., Bräuer, P., Wolke, R., and Herrmann, H.: An advanced modeling study on the  
747 impacts and atmospheric implications of multiphase dimethyl sulfide chemistry, *P. Natl. Acad. Sci. USA*, 113, 11776-11781,  
748 10.1073/pnas.1606320113, 2016.
- 749 Holder, C., Gnanadesikan, A., and Aude-Pradal, M.: Using neural network ensembles to separate ocean biogeochemical and  
750 physical drivers of phytoplankton biogeography in Earth system models, *Geosci. Model Dev.*, 15, 1595-1617, 10.5194/gmd-  
751 15-1595-2022, 2022.

- 752 Hopkins, F. E., Turner, S. M., Nightingale, P. D., Steinke, M., Bakker, D., and Liss, P. S.: Ocean acidification and marine  
753 trace gas emissions, *P. Natl. Acad. Sci. USA*, 107, 760-765, 10.1073/pnas.0907163107, 2010.
- 754 Hopkins, F. E., Archer, S. D., Bell, T. G., Suntharalingam, P., and Todd, J. D.: The biogeochemistry of marine dimethylsulfide,  
755 *Nature Reviews Earth & Environment*, 4, 361-376, 10.1038/s43017-023-00428-7, 2023.
- 756 Huang, B., Liu, C., Freeman, E., Graham, G., Smith, T., and Zhang, H.-M.: Assessment and Intercomparison of NOAA Daily  
757 Optimum Interpolation Sea Surface Temperature (DOISST) Version 2.1, *Journal of Climate*, 34, 7421-7441, 10.1175/jcli-d-  
758 21-0001.1, 2021.
- 759 Huang, S., Poulain, L., van Pinxteren, D., van Pinxteren, M., Wu, Z., Herrmann, H., and Wiedensohler, A.: Latitudinal and  
760 Seasonal Distribution of Particulate MSA over the Atlantic using a Validated Quantification Method with HR-ToF-AMS,  
761 *Environ. Sci. Technol.*, 51, 418-426, 10.1021/acs.est.6b03186, 2016.
- 762 Hulswar, S., Simó, R., Galí, M., Bell, T. G., Lana, A., Inamdar, S., Halloran, P. R., Manville, G., and Mahajan, A. S.: Third  
763 revision of the global surface seawater dimethyl sulfide climatology (DMS-Rev3), *Earth System Science Data*, 14, 2963-2987,  
764 10.5194/essd-14-2963-2022, 2022.
- 765 Humphries, G. R. W., Deal, C. J., Elliott, S., and Huettmann, F.: Spatial predictions of sea surface dimethylsulfide  
766 concentrations in the high arctic, *Biogeochemistry*, 110, 287-301, 2012.
- 767 Johnson, M. T.: A numerical scheme to calculate temperature and salinity dependent air-water transfer velocities for any gas,  
768 *Ocean Science*, 6, 913-932, 10.5194/os-6-913-2010, 2010.
- 769 Keller, M. D., Bellows, W. K., and Guillard, R. R.: Dimethyl sulfide production in marine phytoplankton, in: *Biogenic Sulfur*  
770 in the Environment, edited by: Saltzman, E. S., and Cooper, W. J., ACS Publications, 1989.
- 771 Kettle, A. J., Andreae, M. O., Amouroux, D., Andreae, T. W., Bates, T. S., Berresheim, H., Bingemer, H., Boniforti, R., Curran,  
772 M. A. J., DiTullio, G. R., Helas, G., Jones, G. B., Keller, M. D., Kiene, R. P., Leck, C., Levasseur, M., Malin, G., Maspero,  
773 M., Matrai, P., McTaggart, A. R., Mihalopoulos, N., Nguyen, B. C., Novo, A., Putaud, J. P., Rapsomanikis, S., Roberts, G.,  
774 Schebeske, G., Sharma, S., Simo, R., Staubes, R., Turner, S., and Uher, G.: A global database of sea surface dimethylsulfide  
775 (DMS) measurements and a procedure to predict sea surface DMS as a function of latitude, longitude, and month, *Glob.*  
776 *Biogeochem. Cycles*, 13, 399-444, 10.1029/1999gb900004, 1999.
- 777 Kloster, S., Feichter, J., Maier-Reimer, E., Six, K. D., Stier, P., and Wetzel, P.: DMS cycle in the marine ocean-atmosphere  
778 system—a global model study, *Biogeosciences*, 3, 29-51, 2006.
- 779 Lana, A., Bell, T. G., Simó, R., Vallina, S. M., Ballabrera-Poy, J., Kettle, A. J., Dachs, J., Bopp, L., Saltzman, E. S., Stefels,  
780 J., Johnson, J. E., and Liss, P. S.: An updated climatology of surface dimethylsulfide concentrations and emission fluxes in the  
781 global ocean, *Glob. Biogeochem. Cycles*, 25, GB1004, 10.1029/2010gb003850, 2011.
- 782 Li, H., Zhou, S., Zhu, Y., Zhang, R., Wang, F., Bao, Y., and Chen, Y.: Atmospheric Deposition Promotes Relative Abundances  
783 of High-Dimethylsulfoniopropionate Producers in the Western North Pacific, *Geophys. Res. Lett.*, 48, e2020GL092077,  
784 10.1029/2020GL092077, 2021.
- 785 Longhurst, A. R.: *Ecological Geography of the Sea*, Academic Press, 1998.

- 786 Lovelock, J. E., Maggs, R. J., and Rasmussen, R. A.: Atmospheric Dimethyl Sulphide and the Natural Sulphur Cycle, *Nature*,  
787 237, 452-453, 10.1038/237452a0, 1972.
- 788 Mansour, K., Decesari, S., Ceburnis, D., Ovadnevaite, J., and Rinaldi, M.: Machine learning for prediction of daily sea surface  
789 dimethylsulfide concentration and emission flux over the North Atlantic Ocean (1998-2021), *Sci. Total. Environ.*, 871, 162123,  
790 10.1016/j.scitotenv.2023.162123, 2023.
- 791 Masson-Delmotte, V., Zhai, P., Pirani, A., Connors, S. L., Péan, C., Berger, S., Caud, N., Chen, Y., Goldfarb, L., Gomis, M.  
792 I., Huang, M., Leitzell, K., Lonnoy, E., Matthews, J. B. R., Maycock, T. K., Waterfield, T., Yelekçi, O., Yu, R., and Zhou, R.  
793 e.: IPCC, 2021: Climate Change 2021: The Physical Science Basis. Contribution of Working Group I to the Sixth Assessment  
794 Report of the Intergovernmental Panel on Climate Change, 2021.
- 795 McCoy, D. T., Burrows, S. M., Wood, R., Grosvenor, D. P., Elliott, S. M., Ma, P. L., Rasch, P. J., and Hartmann, D. L.: Natural  
796 aerosols explain seasonal and spatial patterns of Southern Ocean cloud albedo, *Science Advances*, 1, e1500157,  
797 10.1126/sciadv.1500157, 2015.
- 798 McNabb, B. J., and Tortell, P. D.: Improved prediction of dimethyl sulfide (DMS) distributions in the northeast subarctic  
799 Pacific using machine-learning algorithms, *Biogeosciences*, 19, 1705-1721, 10.5194/bg-19-1705-2022, 2022.
- 800 McNabb, B. J., and Tortell, P. D.: Oceanographic controls on Southern Ocean dimethyl sulfide distributions revealed by  
801 machine learning algorithms, *Limnology and Oceanography*, 68, 616-630, 10.1002/lo.12298, 2023.
- 802 McParland, E. L., and Levine, N. M.: The role of differential DMSP production and community composition in predicting  
803 variability of global surface DMSP concentrations, *Limnol. Oceanogr.*, 64, 757-773, 10.1002/lo.11076, 2018.
- 804 Moradkhani, H., DeChant, C. M., and Sorooshian, S.: Evolution of ensemble data assimilation for uncertainty quantification  
805 using the particle filter-Markov chain Monte Carlo method, *Water Resources Research*, 48, 10.1029/2012wr012144, 2012.
- 806 Nightingale, P. D., Malin, G., Law, C. S., Watson, A. J., Liss, P. S., Liddicoat, M. I., Boutin, J., and Upstill-Goddard, R. C.:  
807 In situ evaluation of air-sea gas exchange parameterizations using novel conservative and volatile tracers, *Glob. Biogeochem.  
808 Cycles*, 14, 373-387, 10.1029/1999gb900091, 2000.
- 809 Novak, G. A., Fite, C. H., Holmes, C. D., Veres, P. R., Neuman, J. A., Faloona, I., Thornton, J. A., Wolfe, G. M., Vermeuel,  
810 M. P., Jernigan, C. M., Peischl, J., Ryerson, T. B., Thompson, C. R., Bourgeois, I., Warneke, C., Gkatzelis, G. I., Coggon, M.  
811 M., Sekimoto, K., Bui, T. P., Dean-Day, J., Diskin, G. S., DiGangi, J. P., Nowak, J. B., Moore, R. H., Wiggins, E. B., Winstead,  
812 E. L., Robinson, C., Thornhill, K. L., Sanchez, K. J., Hall, S. R., Ullmann, K., Dollner, M., Weinzierl, B., Blake, D. R., and  
813 Bertram, T. H.: Rapid cloud removal of dimethyl sulfide oxidation products limits SO<sub>2</sub> and cloud condensation nuclei  
814 production in the marine atmosphere, *P. Natl. Acad. Sci. USA*, 118, e2110472118, 10.1073/pnas.2110472118, 2021.
- 815 Omori, Y., Tanimoto, H., Inomata, S., Wada, S., Thume, K., and Pohnert, G.: Enhancement of dimethylsulfide production by  
816 anoxic stress in natural seawater, *Geophys. Res. Lett.*, 42, 4047-4053, 10.1002/2015gl063546, 2015.
- 817 Osman, M. B., Das, S. B., Trusel, L. D., Evans, M. J., Fischer, H., Grieman, M. M., Kipfstuhl, S., McConnell, J. R., and  
818 Saltzman, E. S.: Industrial-era decline in subarctic Atlantic productivity, *Nature*, 569, 551-555, 10.1038/s41586-019-1181-8,  
819 2019.

- 820 Park, K.-T., Lee, K., Kim, T.-W., Yoon, Y. J., Jang, E.-H., Jang, S., Lee, B.-Y., and Hermansen, O.: Atmospheric DMS in the  
821 Arctic Ocean and Its Relation to Phytoplankton Biomass, *Glob. Biogeochem. Cycles*, 32, 351-359, 10.1002/2017gb005805,  
822 2018.
- 823 Park, K. T., Yoon, Y. J., Lee, K., Tunved, P., Krejci, R., Ström, J., Jang, E., Kang, H. J., Jang, S., Park, J., Lee, B. Y., Traversi,  
824 R., Becagli, S., and Hermansen, O.: Dimethyl Sulfide-Induced Increase in Cloud Condensation Nuclei in the Arctic  
825 Atmosphere, *Glob. Biogeochem. Cycles*, 35, e2021GB006969, 10.1029/2021gb006969, 2021.
- 826 Qu, B., Gabric, A. J., Zeng, M., and Lu, Z.: Dimethylsulfide model calibration in the Barents Sea using a genetic algorithm  
827 and neural network, *Environ. Chem.*, 13, 413-424, 10.1071/EN14264, 2016.
- 828 Quinn, P. K., and Bates, T. S.: The case against climate regulation via oceanic phytoplankton sulphur emissions, *Nature*, 480,  
829 51-56, 10.1038/nature10580, 2011.
- 830 Quinn, P. K., Coffman, D. J., Johnson, J. E., Upchurch, L. M., and Bates, T. S.: Small fraction of marine cloud condensation  
831 nuclei made up of sea spray aerosol, *Nat. Geosci.*, 10, 674-679, 10.1038/ngeo3003, 2017.
- 832 Reichstein, M., Camps-Valls, G., Stevens, B., Jung, M., Denzler, J., Carvalhais, N., and Prabhat: Deep learning and process  
833 understanding for data-driven Earth system science, *Nature*, 566, 195-204, 10.1038/s41586-019-0912-1, 2019.
- 834 Saltzman, E. S., Savoie, D. L., Zika, R. G., and Prospero, J. M.: Methane sulfonic acid in the marine atmosphere, *J. Geophys.  
835 Res.*, 88, 10897, 10.1029/JC088iC15p10897, 1983.
- 836 Savoie, D. L., Arimoto, R., Keene, W. C., Prospero, J. M., Duce, R. A., and Galloway, J. N.: Marine biogenic and  
837 anthropogenic contributions to non-sea-salt sulfate in the marine boundary layer over the North Atlantic Ocean, *J. Geophys.  
838 Res.*, 107, 4356, 10.1029/2001jd000970, 2002.
- 839 Screen, J. A., Deser, C., and Simmonds, I.: Local and remote controls on observed Arctic warming, *Geophys. Res. Lett.*, 39,  
840 L10709, 10.1029/2012gl051598, 2012.
- 841 Serreze, M. C., and Barry, R. G.: Processes and impacts of Arctic amplification: A research synthesis, *Global and planetary  
842 change*, 77, 85-96, 2011.
- 843 Sheng, J.-X., Weisenstein, D. K., Luo, B.-P., Rozanov, E., Stenke, A., Anet, J., Bingemer, H., and Peter, T.: Global atmospheric  
844 sulfur budget under volcanically quiescent conditions: Aerosol-chemistry-climate model predictions and validation, *J.  
845 Geophys. Res.-Atmos.*, 120, 256-276, 10.1002/2014jd021985, 2015.
- 846 Sigmund, G., Gharasoo, M., Hüffer, T., and Hofmann, T.: Deep Learning Neural Network Approach for Predicting the  
847 Sorption of Ionizable and Polar Organic Pollutants to a Wide Range of Carbonaceous Materials, *Environ. Sci. Technol.*, 54,  
848 4583-4591, 10.1021/acs.est.9b06287, 2020.
- 849 Simó, R., and Pedrós-Alió, C.: Role of vertical mixing in controlling the oceanic production of dimethyl sulphide, *Nature*, 402,  
850 396-399, 10.1038/46516, 1999a.
- 851 Simó, R., and Pedrós-Alió, C.: Short-term variability in the open ocean cycle of dimethylsulfide, *Glob. Biogeochem. Cycles*,  
852 13, 1173-1181, 10.1029/1999gb900081, 1999b.

- 853 Simó, R., and Dachs, J.: Global ocean emission of dimethylsulfide predicted from biogeophysical data, *Glob. Biogeochem. Cycles*, 16, 1078, 10.1029/2001gb001829, 2002.
- 854 Six, K. D., Kloster, S., Ilyina, T., Archer, S. D., Zhang, K., and Maier-Reimer, E.: Global warming amplified by reduced sulphur fluxes as a result of ocean acidification, *Nat. Clim. Change*, 3, 975-978, 10.1038/nclimate1981, 2013.
- 855 Stefels, J.: Physiological aspects of the production and conversion of DMSP in marine algae and higher plants, *J. Sea. Res.*, 43, 183-197, 2000.
- 856 Stefels, J., Steinke, M., Turner, S., Malin, G., and Belviso, S.: Environmental constraints on the production and removal of the climatically active gas dimethylsulphide (DMS) and implications for ecosystem modelling, *Biogeochemistry*, 83, 245-275, 10.1007/s10533-007-9091-5, 2007.
- 857 Stein, A. F., Draxler, R. R., Rolph, G. D., Stunder, B. J. B., Cohen, M. D., and Ngan, F.: NOAA's HYSPLIT Atmospheric Transport and Dispersion Modeling System, *Bull. Am. Meteorol. Soc.*, 96, 2059-2077, 10.1175/bams-d-14-00110.1, 2015.
- 858 Steiner, N. S., Robert, M., Arychuk, M., Levasseur, M. L., Merzouk, A., Peña, M. A., Richardson, W. A., and Tortell, P. D.: Evaluating DMS measurements and model results in the Northeast subarctic Pacific from 1996–2010, *Biogeochemistry*, 110, 269-285, 10.1007/s10533-011-9669-9, 2011.
- 859 Sunda, W., Kieber, D., Kiene, R., and Huntsman, S.: An antioxidant function for DMSP and DMS in marine algae, *Nature*, 418, 317-320, 2002.
- 860 Tesdal, J.-E., Christian, J. R., Monahan, A. H., and Salzen, K. v.: Evaluation of diverse approaches for estimating sea-surface DMS concentration and air-sea exchange at global scale, *Environ. Chem.*, 13, 390-412, 10.1071/EN14255, 2016.
- 861 Vallina, S. M., and Simó, R.: Strong relationship between DMS and the solar radiation dose over the global surface ocean, *Science*, 315, 506-508, 10.1126/science.1133680, 2007.
- 862 Vogt, M., Vallina, S. M., Buitenhuis, E. T., Bopp, L., and Le Quéré, C.: Simulating dimethylsulphide seasonality with the Dynamic Green Ocean Model PlankTOM5, *J. Geophys. Res.*, 115, 10.1029/2009jc005529, 2010.
- 863 Wang, S., Elliott, S., Maltrud, M., and Cameron-Smith, P.: Influence of explicit *Phaeocystis* parameterizations on the global distribution of marine dimethyl sulfide, *J. Geophys. Res.-Biogeosci.*, 120, 2158-2177, 10.1002/2015jg003017, 2015.
- 864 Wang, W.-L., Song, G., Primeau, F., Saltzman, E. S., Bell, T. G., and Moore, J. K.: Global ocean dimethyl sulfide climatology estimated from observations and an artificial neural network, *Biogeosciences*, 17, 5335-5354, 10.5194/bg-17-5335-2020, 2020.
- 865 Wood, R., Stemmler, J. D., Rémillard, J., and Jefferson, A.: Low-CCN concentration air masses over the eastern North Atlantic: Seasonality, meteorology, and drivers, *J. Geophys. Res. Atmos.*, 122, 1203-1223, 10.1002/2016jd025557, 2017.
- 866 Woolf, D. K.: Bubbles and their role in gas exchange, in: *The Sea Surface and Global Change*, edited by: Liss, P. S., and Duce, R. A., Cambridge University Press, Cambridge, 173-206, 1997.
- 867 Yang, B., Boss, E. S., Haëntjens, N., Long, M. C., Behrenfeld, M. J., Eveleth, R., and Doney, S. C.: Phytoplankton Phenology in the North Atlantic: Insights From Profiling Float Measurements, *Front. Mar. Sci.*, 7, 10.3389/fmars.2020.00139, 2020.
- 868 Yu, L., and Zhou, N.: Survey of imbalanced data methodologies, *arXiv preprint arXiv:2104.02240*, 2021.

- 887 Zhang, X. H., Liu, J., Liu, J., Yang, G., Xue, C. X., Curson, A. R. J., and Todd, J. D.: Biogenic production of DMSP and its  
888 degradation to DMS-their roles in the global sulfur cycle, *Sci. China Life Sci.*, 62, 1296-1319, 10.1007/s11427-018-9524-y,  
889 2019.
- 890 Zhao, J., Ma, W., Bilsback, K. R., Pierce, J. R., Zhou, S., Chen, Y., Yang, G., and Zhang, Y.: Simulating the radiative forcing  
891 of oceanic dimethylsulfide (DMS) in Asia based on machine learning estimates, *Atmos. Chem. Phys.*, 22, 9583-9600,  
892 10.5194/acp-22-9583-2022, 2022.
- 893 Zheng, G., Li, X., Zhang, R. H., and Liu, B.: Purely satellite data-driven deep learning forecast of complicated tropical  
894 instability waves, *Science Advances*, 6, eaba1482, 10.1126/sciadv.aba1482, 2020.
- 895 Zhou, S.: An artificial neural network ensemble model for sea surface DMS simulation, v3.0, Zenodo [Data set],  
896 <https://doi.org/10.5281/zenodo.12398985>, 2024
- 897 Zhou, S., Chen, Y., Huang, S., Gong, X., Yang, G., Zhang, H., Herrmann, H., Wiedensohler, A., Poulain, L., Zhang, Y., Wang,  
898 F., Xu, Z., and Yan, K.: A 20-year (1998-2017) global sea surface dimethyl sulfide gridded dataset with daily resolution, v4.0,  
899 Zenodo [Data set], <https://doi.org/10.5281/zenodo.11879900>, 2024.
- 900 Zhou, S., Chen, Y., Paytan, A., Li, H., Wang, F., Zhu, Y., Yang, T., Zhang, Y., and Zhang, R.: Non-Marine Sources Contribute  
901 to Aerosol Methanesulfonate Over Coastal Seas, *J. Geophys. Res.-Atmos.*, 126, e2021JD034960, 10.1029/2021jd034960,  
902 2021.
- 903 Zindler, C., Bracher, A., Marandino, C. A., Taylor, B., Torrecilla, E., Kock, A., and Bange, H. W.: Sulphur compounds,  
904 methane, and phytoplankton: interactions along a north-south transit in the western Pacific Ocean, *Biogeosciences*, 10, 3297-  
905 3311, 10.5194/bg-10-3297-2013, 2013.
- 906 Zindler, C., Marandino, C. A., Bange, H. W., Schütte, F., and Saltzman, E. S.: Nutrient availability determines dimethyl sulfide  
907 and isoprene distribution in the eastern Atlantic Ocean, *Geophys. Res. Lett.*, 41, 3181-3188, 10.1002/2014gl059547, 2014.
- 908